A carbon-dioxide-based polygeneration system for long-term, large-scale and cross-regional renewable energy applications

This is the ACCEPTED version of this article. The final, published version of the article can be found at: https://doi.org/10.1016/j.rser.2026.116988

Yao Zhao[a,b,*], Shengqi Huang[a], Jian Song[c,d], Christos N. Markides[d], Zhen Huang[a,b,e]

[a] *College of Smart Energy, Shanghai Jiao Tong University, Shanghai 200240, China*

[b] *Shanghai Non-carbon Energy Conversion and Utilization Institute, Shanghai Jiao Tong University, Shanghai 200240, China*

[c] *Birmingham Centre for Energy Storage & School of Chemical Engineering, University of Birmingham, Birmingham B15 2TT, UK*

[d] *Clean Energy Processes (CEP) Laboratory, Department of Chemical Engineering, Imperial College London, London SW7 2AZ, UK*

[e] *Key Laboratory for Power Machinery and Engineering, Ministry of Education, Shanghai Jiao Tong University, Shanghai 200240, China*

Abstract

Multi-energy polygeneration systems offer significant potential to improve energy utilization, enhance operational flexibility and integrate diverse energy sources into advanced infrastructure. This study proposes a long-term, large-scale and cross-regional CO_2-based polygeneration system for energy conversion and management in integrated energy hubs, particularly ports and energy islands. The system integrates a direct air capture module, a carbon dioxide energy storage module and a power-to-fuel module to utilize renewable electricity during charging and to deliver electricity, heating, cooling and transportable fuels during discharging. Thermodynamic models are developed to optimize the system energy, exergy, electricity, heating, cooling and fuel utilization factors, as well as the levelized cost of energy. Under optimal conditions, the system achieves an energy utilization factor of up to 146%, with electricity, heating, cooling and fuel utilization factors of 30%, 79%, 19% and 18%, respectively. The CO_2 secondary distribution coefficient regulates the system's power-to-fuel ratio, while the heat allocation ratio of the high-temperature thermal energy storage governs the overall power-to-heat ratio. The introduction of external waste heat significantly improves the system energy, exergy, electricity and heating utilization factors while reducing the levelized cost of energy from \$0.075/kWh to \$0.039/kWh. High-temperature waste heat primarily enhances electricity output, whereas low-temperature waste heat predominantly increases heating output. Overall, the proposed system can flexibly deliver multiple forms of energy to meet end-user demands. It therefore provides a promising pathway for efficient energy

* Corresponding author: zhaoyao@sjtu.edu.cn

conversion, carbon utilization and sustainable development across diverse application scenarios.

Keywords

Carbon dioxide energy storage; Combined cooling, heating, power and fuel provision; Direct air capture; Polygeneration system; Solid oxide electrolysis cell; Thermal energy storage

Nomenclature

Abbreviations			
CAES	compressed-air energy storage	IC	intercooler
CCHP	combined cooling, heating and power	LAES	liquid-air energy storage
CDES	carbon dioxide energy storage	LHV	low heating value
CES	cold energy storage	LPL	low-pressure liquid storage tank
CHP	combined heating and power	ORC	organic Rankine cycle
CLHS	cascaded latent-heat stores	P2F	power-to-fuel
CON	condenser	PTES	pumped-thermal energy storage
DAC	direct air capture	RH	reheater
EH	electric heater	RWGS	reversible water gas shift
EUF	energy utilization factor	SOEC	solid oxide electrolysis cell
ExUF	exergy utilization factor	TES	thermal energy storage
HHV	high heating value	TMES	thermo-mechanical energy storage
HPL	high-pressure liquid storage tank	TV	throttle valve
HTF	heat transfer fluid	WF	working fluid
HX	heat exchanger		
Greek symbols			
α	heat source coefficient, -	ζ	heat allocation ratio, -
β	discharging power ratio, -	η	efficiency, -
γ	mass flow ratio, -	λ	secondary distribution coefficient, -
δ	primary distribution coefficient, -	μ	dynamic viscosity, Pa·s
ε	effectiveness, -	ρ	density, kg/m^3
ε_p	particle porosity, -		
Symbols			
A_{cell}	electrolysis cell active area, m^2	$\dot{W}$	power rate, W
E	voltage, V	c_p	specific heat capacity, J/(kg·K)
$\dot{E}x$	exergy transfer rate, W	d_p	particle diameter, m
G	Gibbs free energy, J/mol	h	specific enthalpy, J/kg
I	current, A	i	current density, A/m^2
K_p	equilibrium constant, -	i_0	exchange current density, A/m^2
$\dot{N}$	molar flow rate, mol/s	$\dot{m}$	mass flow rate, kg/s
N_{cell}	number of cells in electrolysis stack, -	n	number of stages
P	pressure, Pa	p	partial pressure, Pa
$\dot{Q}$	heat transfer rate, W	q	adsorption loading of sorbent, mol/kg

T	temperature, K	t	time, s or h
$\dot{V}$	volume flow rate, m^3/s	v	velocity, m/s
Superscripts and subscripts			
*	ideal isentropic process	dis	discharging process
0	ambient state	f	working fluid
C	compressor	h	hot fluid
E	expander	i	i-th stage
P	pump	in	inlet
ads	adsorption process	max	maximum
c	cold fluid	out	outlet
char	charging process	vac	vacuum pump
des	desorption process	blo	blower

1. Introduction

The utilization of renewable energy sources is a critical component of the ongoing global energy transition [1]. Technologies such as wind and solar energy offer significant potential because of their abundance and environmental benefits. However, their inherent intermittency and variability present challenges for large-scale integration. These fluctuations highlight the need for innovative energy storage and conversion technologies to ensure grid stability and a reliable energy supply, particularly for power balancing and advanced energy management [2].

At the same time, energy consumption patterns are evolving with increasingly diverse demand profiles. While traditional energy systems primarily focused on electricity supply to industrial, commercial and residential sectors, advancements in technology and sustainability have broadened the scope [3]. Modern energy systems now require integrated solutions capable of simultaneously producing, storing and distributing multiple energy vectors, such as electricity, heating, cooling and fuels, across various sectors [4]. This trend is especially important in specialized applications like offshore ports and energy islands, where energy systems must be flexible, resilient and autonomous [5]. These locations need not only reliable electricity but also cooling for logistics, heating for operations and clean fuels for transportation. Their geographic and operational constraints demand long-term, large-scale and cross-regional energy storage capabilities. Consequently, integrated multi-energy polygeneration systems are becoming essential to meet the complex demands of these frontier energy environments and to ensure sustainable and resilient energy infrastructures.

To address the diverse energy demands in renewable-dominated scenarios, polygeneration systems driven by energy storage have attracted growing attention. Among the emerging solutions, thermo-mechanical energy storage (TMES) technologies [6], such as compressed-air energy storage (CAES) [7], liquid-air energy storage (LAES) [8], pumped-thermal energy storage (PTES) [9] and carbon dioxide energy storage (CDES) [10], stand out due to their capability for large-scale energy storage. These systems convert electrical energy into mechanical or thermal energy during charging and reverse this process during discharging [11]. Their versatility in handling multiple energy forms makes them particularly suitable for integration into combined cooling, heating and power (CCHP) systems [12].

In particular, CDES uses CO_2 as the working fluid, leveraging its high energy density, excellent heat transfer, low viscosity and ability to be stored as a liquid under near-ambient conditions. These properties make CDES not only an efficient storage medium but also a carbon buffer that decouples capture and utilization in time. When integrated with direct air capture (DAC) and power-to-fuel (P2F) subsystems, CDES forms a carbon conversion chain that links capture, storage and fuel synthesis, and delivers electricity, heating, cooling and fuel within a unified platform.

Such polygeneration systems typically comprise three interlinked modules: DAC, CDES and P2F. During the charging phase, surplus electricity, often from renewable sources, is converted and stored in the form of thermal and mechanical energy within the CDES module. In the discharging phase, this stored energy is flexibly released as electricity, heating, cooling and fuel. The carbon dioxide is first captured from the

atmosphere via the DAC module, then directed into the CDES module for intermediate storage, and finally utilized in the P2F module to synthesize highly valuable fuels such as methane, methanol or Fischer-Tropsch products. This integrated configuration not only facilitates energy vector diversification but also supports renewable energy
smoothing, long-duration storage and carbon circularity.

However, integrating such systems involves complex interactions among multiple energy forms and mass flows, resulting in highly coupled system behavior. To date, no comprehensive studies have addressed the modeling and analysis of such fully integrated polygeneration systems. To bridge this gap, this study proposes a long-term, large-scale and cross-regional CO_2-based polygeneration system that simultaneously delivers electricity, heating, cooling and fuel. As illustrated in Fig. 1, the system is designed to mitigate the spatiotemporal mismatch between intermittent renewable energy supply and diverse end-use energy demands. The core objective is to establish a carbon conversion chain that provides multi-energy services while enabling negative-carbon operation through the integrated coupling of carbon capture, energy storage and fuel utilization.

A thermodynamic model is developed to evaluate eight critical operational parameters: CO_2 mass flow rate, inter-module allocation ratio, adsorption temperature, desorption temperature, compression and expansion stage configuration, heat allocation ratio, solid oxide electrolysis cell (SOEC) parameters and external waste heat characteristics. Dual-scenario optimization (with and without waste heat integration) evaluates seven performance dimensions: energy, exergy, electricity, heating, cooling and fuel utilization factors, as well as the levelized cost of energy (*LCOE*). This study reveals the fundamental energy conversion mechanisms within the system and clarifies how system configurations and operating parameters are optimized according to different performance objectives. The proposed design offers a novel pathway for efficient renewable energy utilization, deep carbon integration and multifunctional energy outputs, making it well suited for offshore ports, energy islands and other emerging application scenarios.

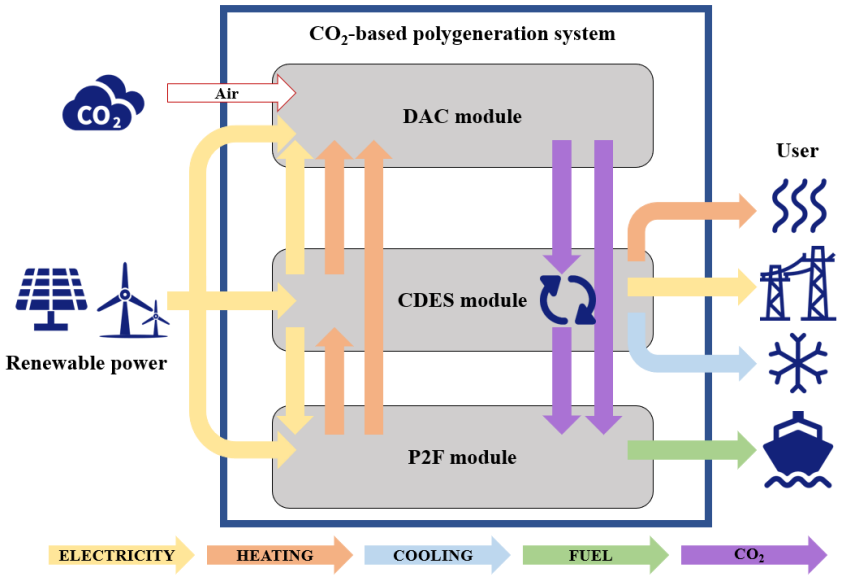


Fig. 1. CO_2-based polygeneration system framework.

This article is organized as follows. Section 2 presents a detailed literature review of DAC, CDES and P2F technologies, highlighting their current development status as well as the challenges and opportunities associated with their integration. Section 3 introduces the operational principles of the proposed polygeneration system, explaining the system configuration and energy flow. Section 4 describes the mathematical models and performance indicators used to evaluate the system, including the assumptions made for simulation and optimization. Section 5 discusses the simulation results and evaluates the technical and economic performance of the system under various scenarios. Finally, Section 6 concludes the article by summarizing the key findings and offering suggestions for future research.

2. Literature review

2.1 Direct air capture

DAC captures CO_2 directly from ambient air, providing a sustainable carbon source that can subsequently be stored or utilized [13]. As a technology capable of extracting low-concentration CO_2 (~400 ppm), DAC offers flexibility and is well suited for remote or energy-constrained locations such as islands and ports [14]. When integrated with carbon storage and utilization pathways, DAC can enable net-negative emissions and contribute to an integrated carbon conversion chain [15].

DAC generally operates through two main approaches: high-temperature liquid solvents [16] and low-temperature solid sorbents [17]. In the liquid solvent approach, CO_2 is absorbed using alkaline hydroxides and later released through thermal decomposition at temperatures between 800 °C and 900 °C. This process is highly energy-intensive. Alternatively, solid sorbent-based methods for CO_2 capture include techniques such as temperature swing adsorption [18], pressure-vacuum swing adsorption [19] and temperature-vacuum swing adsorption [20]. In these systems, selectivity is often enhanced by functionalizing the sorbents with amine groups [21] or by using covalent organic frameworks [22].

While DAC technologies are advancing from laboratory research to pilot-scale and commercial deployment, they still face challenges, particularly high energy consumption [23]. Liquid solvent regeneration requires high-temperature heat (800-900 °C) [24], whereas solid sorbents operate at lower temperatures (80-120 °C) but still demand a continuous heat input [25]. To improve efficiency and reduce costs, DAC systems are increasingly integrated with waste heat recovery, solar thermal energy, heat pumps and thermal energy storage (TES) solutions [26].

Fahr et al. [27] evaluated the integration of DAC with various renewable energy sources, including solar, wind, biomass, geothermal and nuclear power, and demonstrated the feasibility of large-scale carbon capture for each of them. Mohan et al. [28] demonstrated that extracting ~10% of low-pressure steam from nuclear turbines meets the heat requirements for DAC, enabling 1 GW plants to capture one million tons of CO_2 annually. Similarly, Bertoni et al. [29] found that small modular reactors improve the thermal utilization ratio from 32% to 85% when combined with DAC. Other studies have explored integrating DAC with solar thermal systems, industrial waste heat and high-temperature heat pumps to reduce energy use to 2.8 GJ/t CO_2 [30].

Among various energy integration pathways, nuclear- and geothermal-powered DAC systems offer high thermal efficiency and reliability but face infrastructure and public acceptance challenges [27]. In contrast, solar- or waste-heat-powered DAC systems provide flexible deployment options but are limited by variability or site-specific availability [31]. Economic analyses suggest that integration with nuclear or geothermal can lower CO_2 removal costs to \$200–\$300/t CO_2, compared to \$600/t CO_2 for natural gas-driven DAC [32].

Despite the increasing interest in integrating DAC with various thermal and renewable systems, existing studies focus primarily on coupling DAC with external heat sources to facilitate CO_2 capture, followed by either carbon sequestration or utilization. However, these approaches often overlook the broader system-level dynamics and interdependencies involved in the full CO_2 conversion chain from atmospheric capture through intermediate storage and energy integration to downstream utilization in multi-energy production. A more holistic perspective is therefore essential to unlock the full potential of DAC as a core component in future carbon-neutral energy systems.

2.2 Carbon dioxide energy storage

CDES functions as a multifunctional system that bridges carbon capture and utilization [33]. CDES utilizes CO_2 as both a carbon carrier and a working fluid. This facilitates the temporal decoupling between CO_2 capture and downstream processes, and enhances the operational flexibility and stability of integrated energy systems [34]. Depending on the pressure and temperature conditions within the storage tanks, CO_2 can be maintained in various thermodynamic states, such as the supercritical [35] or liquid state [36]. This versatility in CO_2 storage enables tailored energy-management strategies that respond effectively to system demands and external load fluctuations. As a result, the overall operational efficiency and reliability of the system can be improved [37].

In recent years, considerable research efforts have focused on advancing the thermodynamic performance and optimization of CDES systems. Hao et al. [38] explored the use of multiple heat transfer fluids for staged thermal storage, optimizing the heat transfer performance of the system. Their work achieved a roundtrip efficiency of 76% and a thermal utilization efficiency of 96%. Liu et al. [39] conducted a comparative study of CO_2 liquefaction and storage strategies. They found that systems employing throttling-based cooling for CO_2 liquefaction combined with isochoric storage achieved the best performance, with a roundtrip efficiency of 72% and a levelized cost as low as \$0.11/kWh. Sun et al. [40] proposed the use of liquid methanol for sensible cold storage together with a latent cold storage unit, which broadens the application scenarios of CDES.

Dynamic performance analysis is crucial for accurately evaluating CDES operation under real-world conditions. Huang et al. [41] developed a dynamic model for CDES and revealed significant discrepancies compared to steady-state simulations. They found that the electricity and heating outputs estimated by the steady-state model were over three times higher than those of the dynamic model. Furthermore, the roundtrip efficiency of the dynamic model (55%) was notably lower than that of the steady-state model (69%), primarily because during actual dynamic operation, the storage pressures in the high- and low-

pressure tanks fluctuate over time. These pressure variations alter the compression and expansion ratios, leading to continuous changes in both the performance and mass flow rates of the compressor and expander. Hao et al. [42] also investigated the dynamic response curves of high-pressure liquid CO_2 tanks during depressurization, providing important insights for the design and safe operation of CDES systems. Under variable-pressure operating conditions, increasing the mass flow rate of CO_2 can reduce the roundtrip efficiency, but it significantly enhances the energy storage density [43]. Zhao et al. [44] investigated the overall performance and found that the roundtrip efficiencies under constant-pressure and variable-pressure modes were 65% and 67%, respectively.

CDES can also be coupled with external heat sources to improve overall system performance [45]. Heat sources can include solar thermal collectors, waste heat from gas turbine exhaust, residual heat from nuclear power plants and other similar sources [46]. Xu et al. [47] showed that coupling geothermal energy with CDES raises the turbine inlet temperature during discharge, significantly improving the roundtrip efficiency and lowering the levelized cost of electricity. Solar thermal integration reduces grid fluctuations [48] while increasing power output [49]. Coupling CDES with high-temperature TES enables the use of surplus renewable electricity, improving system flexibility under variable power quality [50].

Building upon the foundational studies of CDES, recent research has extended its application beyond simple charge-discharge operation toward delivering multiple forms of energy. The first step in this evolution has been the development of combined heat and power (CDES-CHP) systems, in which surplus heat from the thermal storage tank or from the outlet of the last-stage expander is recovered for external heating. Hao et al. [51] developed a CDES-CHP configuration achieving a roundtrip efficiency of 67% and an energy efficiency of 88%. Xu et al. [52] proposed a CDES-CHP system coupled with a gas turbine cycle and CO_2 capture, which reached an energy efficiency of 63% and an *LCOE* of \$0.087/kWh. These studies demonstrated that CDES can effectively provide not only electricity but also valuable thermal energy, laying the foundation for multi-energy applications.

It is worth noting that the distinction between CHP and CCP modes in CDES is primarily determined by the temperature at the outlet of the last-stage expander, which depends on system operating parameters. When this temperature exceeds the ambient temperature, surplus heat can be recovered for heating, and the system operates in CHP mode. In contrast, when the temperature is lower than ambient temperature, surplus cold energy can be recovered for cooling, leading to CCP operation. Building on this concept, research has moved toward combined cooling and power (CDES-CCP) systems, which utilize cold energy recovered from CO_2 expansion for external cooling. Sun et al. [53] developed a CDES-CCP system that operates without additional heat or cold sources. In this configuration, a regenerator was incorporated into the discharge process, which lowered the temperature at the outlet of the last-stage expander and allowed surplus cold energy to be extracted from an ice-water mixture pool. The system achieved an energy efficiency of 79%, an exergy efficiency of 58% and a total cost per unit of energy output of \$0.15/kWh. Wang et al. [54] proposed a CDES-CCP configuration based on gas-liquid phase change, where cooling during charging was supplied by a refrigeration cycle and cooling during discharging was provided by the cold CO_2 at the outlet of the last-stage expander, achieving an energy efficiency of 112%

and a total cost per unit of energy output of $0.10/kWh.

The most recent and advanced stage of this progression is combined cooling, heating and power (CDES-CCHP) systems, which integrate both heating and cooling functions alongside power generation within a single platform. In such systems, heating is primarily derived from CO_2 compression, while cooling originates from CO_2 expansion. However, CDES-CCHP systems face challenges related to the cooling-to-power ratio. Liu et al. [55] addressed this by demonstrating adjustable capacities through variations in pressure and temperature parameters. Throttle valve integration also enables the decoupling of cooling [56], and Deng et al. [57] achieved a remarkable energy efficiency of 320% through parallel loop configurations. Supercritical CO_2 storage integration reduces throttling losses [58], while ejector-based designs further enhance system flexibility [59].

Current research on CDES predominantly centers on closed-loop analyses, focusing on internal CO_2 cycling and thermodynamic optimization. Most multi-energy applications studied to date have been limited to CDES-CHP, CDES-CCP or CDES-CCHP configurations, with little attention given to integrating additional energy forms such as fuels. Furthermore, the potential of CDES as a bridging element within an open-loop carbon management chain linking carbon capture, storage and utilization has yet to be fully explored. Few studies have addressed the system-level interactions between CDES and upstream and downstream technologies. A more integrated perspective is therefore essential to unlock the full value of CDES in future carbon-neutral multi-energy systems.

2.3 Power-to-fuel

The P2F pathway enables the utilization of CO_2 either captured directly from emission sources or retrieved from carbon storage systems, converting it into storable and transportable fuels using renewable electricity [60]. This approach not only promotes CO_2 recycling but also offers sustainable energy carriers for the transportation and industrial sectors [61]. Conventional P2F processes typically involve two sequential stages: (1) the electrolysis of water using renewable electricity to generate H_2 and (2) the catalytic synthesis of fuels such as methane [62], methanol [63], dimethyl carbonate [64] or Fischer-Tropsch hydrocarbons [65] through reaction with captured CO_2. While these technologies are considered technically mature, they still face significant challenges, such as high overall energy demand [66] and issues related to hydrogen storage and transportation [67].

SOEC offers an efficient alternative by co-electrolyzing CO_2 and H_2O to directly produce syngas (H_2 + CO), with a tunable H_2:CO ratio suitable for fuel synthesis in a single step [68]. Operating at temperatures between 773 K and 1273 K, SOECs benefit from enhanced reaction kinetics and reduced electrical energy input [69]. Compared to conventional alkaline and proton exchange membrane electrolysis, SOECs are better suited for thermal integration and can theoretically achieve nearly 100% electrical efficiency [70]. Co-electrolysis in SOECs also results in lower area-specific resistance, improving electrochemical performance compared with separate H_2O and CO_2 electrolysis [71]. The all-solid-state design of SOECs supports reversible operation as solid oxide fuel cells, enabling flexible two-way conversion between electrical and chemical energy [72]. This versatility promotes their integration into hybrid energy systems [73].

Current research in SOEC technology mainly focuses on the following aspects: (1) reaction mechanisms and performance optimization of co-electrolysis [74], (2) syngas composition control to ensure compatibility with downstream processes [75] and (3) catalyst development and thermal coupling for methanation [76]. CO in SOEC syngas is primarily produced via the reverse water gas shift (RWGS) reaction, with significant direct CO_2 electrolysis occurring at high current densities [77]. By adjusting electrode materials and operating conditions, SOECs can flexibly tailor the H_2:CO ratio to meet the requirements of downstream synthesis [78].

System-level optimization of SOECs focuses on operating parameters such as temperature [79], inlet gas composition [80] and operating voltage [81] to increase current density and syngas yield. Moreover, integrating SOECs with external heat sources or recovering internal waste heat can enhance overall efficiency and energy recovery. This provides a promising route for efficient renewable energy conversion and fuel production [82].

Compared with the conventional two-step process of water electrolysis followed by syngas synthesis, the SOEC approach streamlines the pathway by eliminating intermediate stages. However, it also imposes stricter requirements on thermal management and waste heat recovery, which makes system integration more challenging.

Current P2F research largely centers on the direct use of CO_2 sourced from carbon capture outlets for fuel production, frequently neglecting the variability in CO_2 supply at this point. This limitation highlights the critical need for incorporating a CO_2 storage module to buffer supply fluctuations and ensure consistent fuel output. Moreover, the thermal storage tanks within the CO_2 energy storage system offer a promising approach to efficient thermal management and address one of the key challenges in integrating SOEC-based P2F systems. Addressing these challenges is vital to improving the reliability, scalability and overall performance of P2F technologies in practical applications.

2.4 Integrated system

The integration of DAC, CDES and P2F technologies enables a complete carbon conversion chain while supporting polygeneration. Among them, the coupling of DAC and P2F has garnered increasing attention in recent studies, with particular focus on thermal integration strategies [83]. Researchers have shown that low-grade heat recovered from P2F units can drive the desorption process in DAC. Such integration can achieve internal thermal self-sufficiency, reduce thermal losses, improve carbon utilization, and significantly enhance overall system efficiency [84].

Paulsen et al. [85] employed a high-temperature liquid solvent DAC to capture CO_2, which was subsequently converted into jet fuel via Fischer-Tropsch synthesis using electrolytic hydrogen. The authors evaluated five system configurations and found that the solid oxide electrolysis cell (SOEC)-based design achieved the highest heat recovery efficiency of 85%. However, economic analysis showed negative net present values for all scenarios, with the lowest levelized cost of fuel at €4.45/L, highlighting the need for further cost reduction. Similarly, Emadi et al. [86] proposed a system in which captured CO_2 and steam are co-electrolyzed in a SOEC to produce syngas, which can then be converted into either methanol or

synthetic fuels, depending on the downstream process selection. The system was designed to capture 250,000 tons of CO_2 annually, with levelized production costs of $1320/ton for methanol and $2780/ton for synthetic fuels. In contrast, Furst et al. [87] used a low-temperature solid sorbent DAC and demonstrated that integrating low-grade heat from the P2F process into the DAC regeneration step could achieve an energy efficiency of 75%. Zhang et al. [88] investigated the thermal integration of DAC, alkaline water electrolysis and methanol synthesis. Compared to a nonintegrated configuration, the energy demand for methanol production was reduced from 50 GJ/ton to 38 GJ/ton, with an overall system energy efficiency of 53% and a levelized cost of methanol of just over $800/ton.

Some studies have gone further by exploring the tri-coupling of DAC, CDES and P2F systems. These configurations leverage CDES technologies not only as a buffer for CO_2 flow and pressure but also as a thermal energy storage mechanism. This helps stabilize the intermittent output of renewable energy and improves overall system flexibility. The stored CO_2 can be directly used for downstream fuel synthesis, and the carbon conversion chain is thus completed. Moreover, during the charging and discharging processes, the CDES unit may provide useful heating or cooling that can be redistributed to DAC or P2F modules. This enables multi-energy integration and reduces the external energy input. Song et al. [89] proposed a system integrating flue gas CO_2 capture, CDES and dry reforming of methane. In this system, the reforming reaction heat is partially used to enhance CDES power output and partially used to regenerate captured CO_2. Under this configuration, the system achieves a 220% roundtrip efficiency and a 25% internal rate of return (IRR). Qi et al. [90] demonstrated the use of CO_2 storage in CDES as a buffer to support water electrolysis for hydrogen production. The hydrogen reacts with CO_2 to form methane. The integrated system coproduces electricity, hydrogen and methane with an energy efficiency of 41%. The projected cost of methane by 2050 is ~€100/kWh. These integrated systems hold promise for deployment in regions with high renewable energy penetration and strong decarbonization demands, such as offshore ports and energy islands.

Despite notable progress, current research on integrated systems typically focuses on fuel or electricity output, overlooking the potential of CDES to deliver heating and cooling externally. This limits the full exploitation of its multi-energy output capability, which is essential for enhancing system-wide flexibility and cross-sector integration. Therefore, future research should adopt a holistic perspective that fully leverages all energy forms, including electricity, heating, cooling and fuel, in order to optimize the performance and versatility of integrated carbon-conversion systems and enable the external delivery of high-value-added energy products across sectors.

2.5 Critical analysis of the state-of-the-art and identification of gaps

Despite significant progress in each module, critical gaps persist throughout the carbon conversion chain. Research on DAC has largely focused on thermal integration with external heat sources [91], without fully capturing the dynamic interactions spanning from CO_2 capture and intermediate storage to downstream multi-energy production. Studies on CDES primarily concentrate on closed-loop thermodynamic optimization [92], with limited exploration of its potential role as an open-loop buffer linking capture,

storage and utilization processes, and they have so far focused mainly on CDES-CHP, CDES-CCP or CDES-CCHP configurations, without extending to polygeneration schemes that also incorporate fuel production. Similarly, P2F research tends to focus on the direct conversion of CO_2 from capture outlets into fuels [93], often overlooking fluctuations in CO_2 supply and the opportunity to leverage thermal storage within CO_2 tanks for enhanced heat management. Even studies of integrated systems, although they move beyond analyses of individual components, generally prioritize fuel or electricity outputs and fail to fully consider the capacity of CDES to provide both heating and cooling.

These gaps collectively reveal a broader research deficiency: the lack of holistic modeling frameworks that capture the spatiotemporal coordination and synergistic operation of fully integrated CO_2-based polygeneration systems. Such systems involve tightly coupled electricity, heating, cooling and fuel flows, along with interacting mass streams and intermediate storage. Existing studies often isolate individual modules or emphasize specific outputs, and thus fall short of capturing the full complexity and integration potential of a unified cross-domain framework. Moreover, economic assessments, particularly those incorporating metrics such as the *LCOE*, remain scarce, limiting the ability to evaluate cost-effectiveness alongside technical performance and hindering the identification of economically viable configurations for large-scale deployment.

In this context, the CO_2-based polygeneration system proposed in this work serves as a conceptual framework highlighting the potential of integrated carbon capture, storage and utilization. By forming a complete carbon conversion chain that spans capture (DAC), intermediate storage and regulation (CDES) and high-value utilization (P2F), the system not only achieves carbon circularity but also enables flexible outputs of electricity, heating, cooling and fuel. Although implementation challenges remain, the multi-energy flexibility of the proposed system enhances its compatibility with renewable energy integration, localized demand response and cross-sector coupling. Furthermore, by incorporating economic indicators such as the *LCOE* into the assessment, the framework enables a comprehensive evaluation of both the technical and economic performance of the proposed system in comparison with other polygeneration systems discussed in Section 5.8, thereby positioning the carbon conversion chain as a promising reference architecture for future carbon-neutral energy systems.

3. System description

Fig. 2 illustrates the proposed CO_2-based polygeneration system, which integrates the DAC, CDES and P2F modules. The system operates at approximately 10 MW and consists of two main phases: charging and discharging.

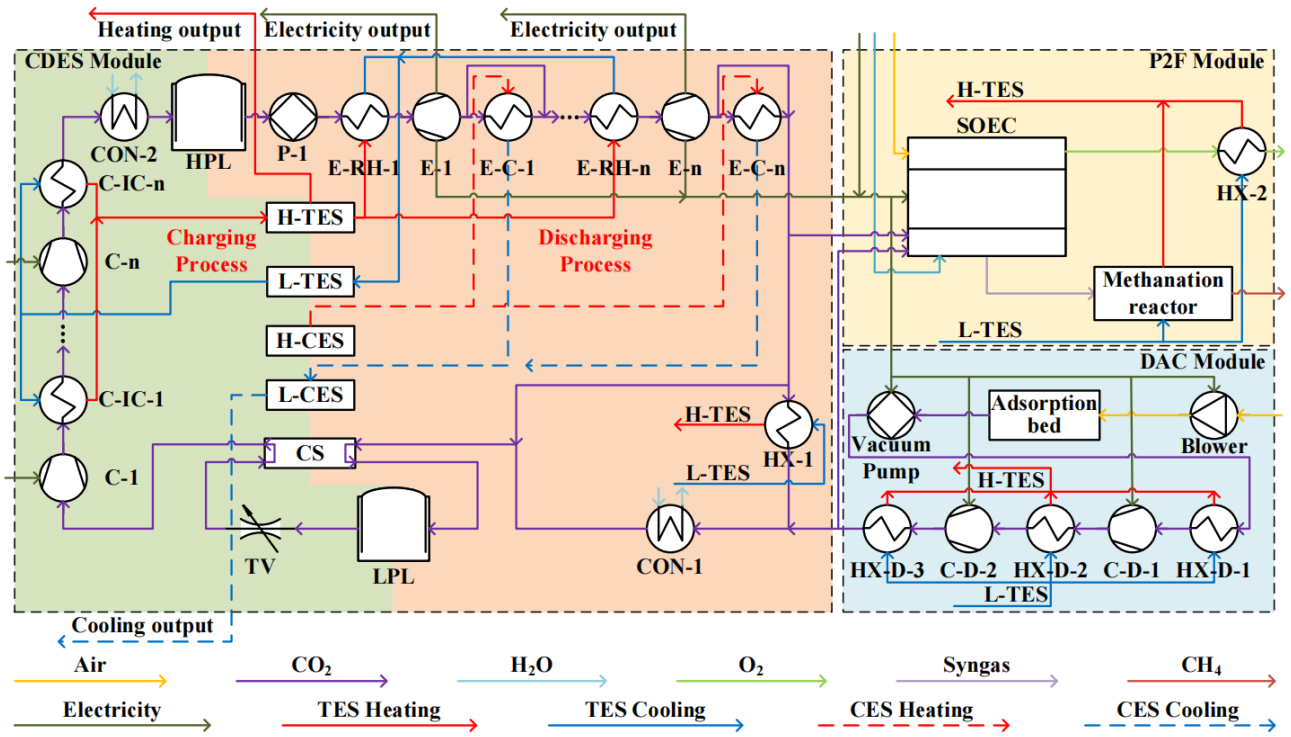


Fig. 2. Schematic diagram of the proposed CO_2-based polygeneration system. (C: Compressor, E: Expander, P: Pump, TV: Throttle valve, HX: Heat exchanger, CON: Condenser, H-TES: High-temperature thermal energy storage, L-TES: Low-temperature thermal energy storage, H-CES: High-temperature cold energy storage, L-CES: Low-temperature cold energy storage, CS: Cold storage, LPL: Low-pressure liquid storage tank, HPL: High-pressure liquid storage tank, HX-D: Heat exchanger in the DAC module, C-D: Compressor in the DAC module, C-IC: Intercooler in the compression process, E-RH: Reheater in the expansion process, E-C: Heat exchangers for cold storage in the expansion process, TES Heating: Flow of high-temperature heat transfer fluid associated with the H-TES, TES Cooling: Flow of low-temperature heat transfer fluid associated with the L-TES, CES Heating: Flow of high-temperature cold fluid associated with the H-CES, CES Cooling: Flow of low-temperature cold fluid associated with the L-CES.)

Charging process: During off-peak hours, CO_2 captured via DAC is introduced into the system. A portion is routed to the P2F module, where it is co-electrolyzed with high-temperature steam in the SOEC to produce syngas, which is then converted into methane. The remaining CO_2 serves as the working fluid in the CDES module. In the CDES module, CO_2 transfers thermal energy to the high-temperature thermal energy storage (H-TES) and absorbs cold energy from the cold storage (CS), where it liquefies in the low-pressure liquid storage tank (LPL). The liquefied CO_2, along with recirculated CO_2 from the CS, is compressed in multiple stages. Each compression stage uses intercoolers (C-IC) to transfer recovered heat to the H-TES. After final compression and heat recovery, the CO_2 is condensed into a high-pressure liquid and stored in the high-pressure liquid storage tank (HPL).

Discharging process: During peak demand, the CO_2 stored in the HPL is passed through the reheater (E-RH), where it absorbs thermal energy from the H-TES before driving multi-stage expansion turbines to generate electricity. CO_2 exiting each expander (E) is routed based on its temperature. If the outlet

temperature is below ambient, the CO_2 flows through heat exchangers for cold storage (E-C) to store cold energy in the L-CES. Otherwise, it moves to the next reheater for further expansion. The final-stage expanded CO_2 is sent to the P2F module, where it is co-electrolyzed together with the CO_2 from the CDES module. Synthetic methane is then produced. CO_2 exiting E-C-n continues to the CDES module, where its thermal management depends on its temperature. If it is above ambient, it transfers thermal energy through HX-1 for heat recovery, then absorbs cold energy from the CS. If it is below ambient, it directly enters the CS for cooling. The liquefied CO_2 is stored in the LPL. This completes the cycle and prepares the system for the next charging process.

SOEC component operation (see Fig. 3): Thermal energy from the cathode and anode exhaust streams preheats the incoming fluid, with excess heat from the anode stored in the H-TES. An electric heater (EH4) raises the temperature of the syngas from the cathode outlet to the required level for methanation. All thermal energy is stored in the H-TES. It is used for two purposes: direct heating applications and reheating CO_2 at the expander inlets to boost electricity generation efficiency. CO_2 exiting the expander at below-ambient temperatures is directed to the L-CES to provide cooling.

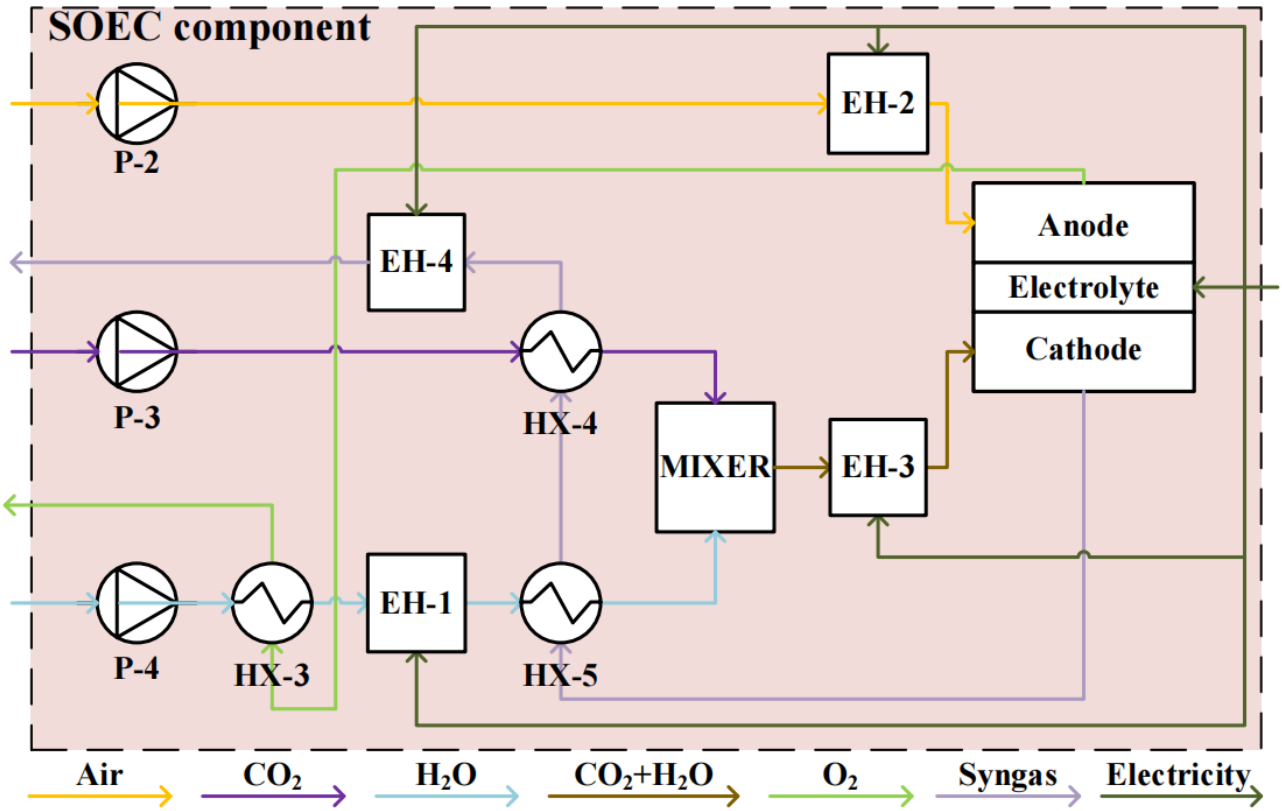


Fig. 2. Schematic diagram of the SOEC component layout and interconnections (EH: Electric heater).

The system dynamically regulates CO_2 flow and heat allocation in the H-TES. This enables adaptive co-generation of electricity, heating, cooling and fuel to meet end-user needs.

4. Methodology

The research methodology adopted in this study is illustrated in Fig. 4. It encompasses three main parts:

model development, parameter analysis and optimization. Specifically, detailed mathematical models of DAC, CDES and P2F modules are developed with integrated energy and mass coupling. Subsequently, the effects of key parameters on system performance are analyzed. Finally, single-objective optimizations targeting different performance metrics are conducted based on the first law of thermodynamics, the second law of thermodynamics and economic considerations.

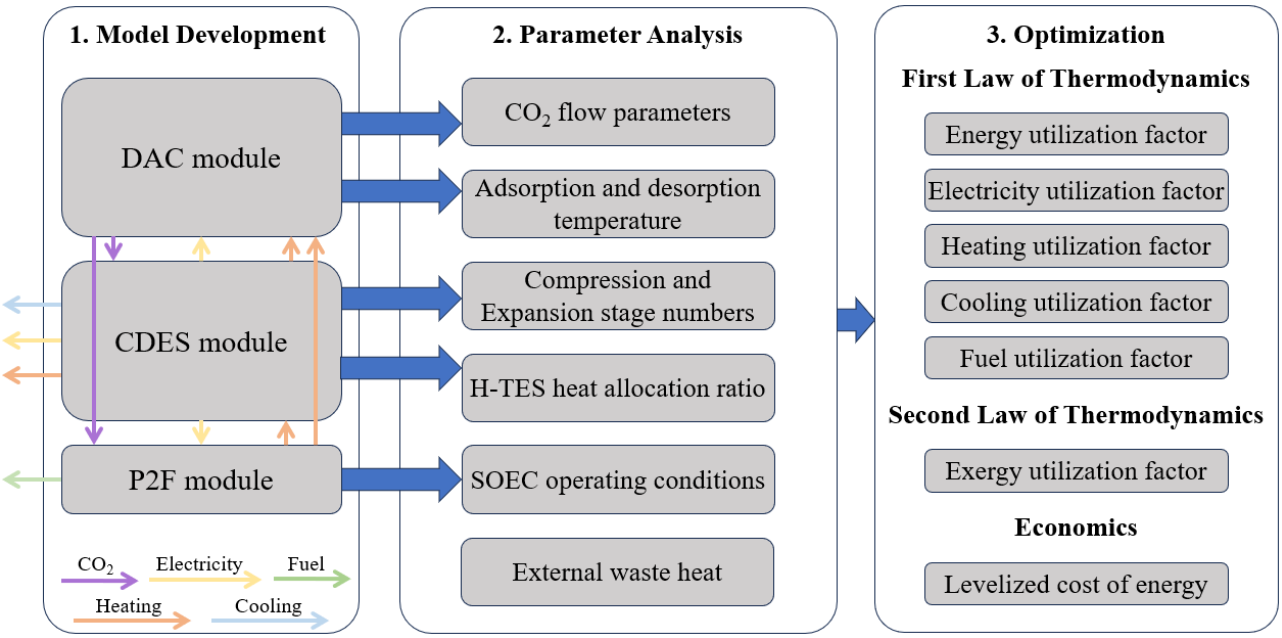


Fig. 3. Research methodology flowchart for the proposed CO_2-based polygeneration system modeling, performance evaluation and optimization process.

This study is a theoretical work focused on steady-state thermodynamic modeling of the proposed system. All simulations were carried out using MATLAB (R2023a), which offers a flexible environment for equation-based modeling and numerical computation. Thermophysical properties of the working fluids were obtained from the REFPROP 9.1 database developed by NIST, which ensures high-accuracy data for real-gas behavior. The combination of MATLAB and REFPROP provides both computational efficiency and reliable property estimation, making it well suited for the system-level energy analyses conducted in this work.

This section describes the modeling framework for the proposed system, using the following assumptions:

(1) Pressure losses in tanks, heat exchangers, condensers, electric heaters and pipelines are neglected.

(2) Constant pressure ratios are maintained across all compression and expansion stages.

(3) Mechanical losses, as well as changes in potential and kinetic energy, are disregarded.

(4) Steady-state operation governs system simulations.

(5) HPL/LPL pressures and temperatures remain invariant during charging/discharging.

(6) TES/CES units operate adiabatically during energy storage/release.

(7) Compressors, expanders and pumps exhibit 85% isentropic efficiency [94, 95] and heat exchangers

maintain an effectiveness of 0.90 [95].

(8) The SOEC operates continuously at 1073 K [96].

(9) Electrochemical mechanisms in the SOEC focus on CO_2-H_2O co-electrolysis and RWGS reactions.

(10) Catalytic methanation achieves 95% CO_2-to-CH_4 conversion efficiency under the simulation parameters [97, 98].

The component models are developed on the basis of the first law of thermodynamics and the law of mass conservation.

4.1 Direct air capture module

The DAC module comprises multiple parallel adsorption units. The primary energy consumption of the system includes electric power for blower operation (Eq. (1)) and vacuum pump activation (Eq. (2)), alongside thermal energy for adsorbent regeneration heating (Eq. (3)), CO_2 thermal conditioning (Eq. (4)) and desorption enthalpy (Eq. (5)) [99, 100]:

$$\dot{W}_{\mathrm{blo}} = \Delta P \dot{V}_{\mathrm{air}} \tag{1}$$

$$\dot{W}_{\mathrm{vac}} = \left(RT_{\mathrm{vac}} / \eta_{\mathrm{P}} \right) \ln \left(P_0 / P_{\mathrm{des}} \right) \tag{2}$$

$$\dot{Q}_{\mathrm{abs}} = \dot{m}_{\mathrm{abs}} c_{\mathrm{p,ads}} \left(T_{\mathrm{des}} - T_{\mathrm{ads}} \right) \tag{3}$$

$$\dot{Q}_{\mathrm{CO_2}} = \dot{m}_{\mathrm{CO_2}} c_{\mathrm{p,CO_2}} \left(T_{\mathrm{des}} - T_{\mathrm{ads}} \right) \tag{4}$$

$$\dot{Q}_{\mathrm{des}} = -\Delta H_{\mathrm{CO_2}} \dot{n}_{\mathrm{CO_2}} \tag{5}$$

where ΔP is the pressure drop across the adsorbent bed, $\dot{V}_{\mathrm{air}}$ is the volumetric air flow rate, ΔH is the adsorption enthalpy, η_{P} is the pump isentropic efficiency, and the subscripts "vac", "ads" and "des" denote the vacuum pump, adsorption process and desorption process, respectively.

The pressure drop in Eq. (1) is calculated using the Ergun equation [101]:

$$\Delta P = \frac{150 \mu_{\mathrm{g}} L_{\mathrm{bed}} \left(1-\varepsilon\right)^2 v_{\mathrm{s}}}{d_{\mathrm{p}}^2 \varepsilon_{\mathrm{p}}^3} + \frac{1.75 L_{\mathrm{bed}} \rho_{\mathrm{g}} \left(1-\varepsilon\right) v_{\mathrm{s}}^2}{d_{\mathrm{p}} \varepsilon_{\mathrm{p}}^3} \tag{6}$$

where μ_{g} and ρ_{g} represent the air dynamic viscosity and density, respectively, L_{bed} indicates the adsorbent bed length, v_{s} denotes the superficial air velocity, while d_{p} and ε_{p} correspond to the particle diameter and porosity.

This study employs mmen-Mg_2(dobpdc) as the porous adsorption material. The key thermal and structural properties of the material are provided in Table 1.

Table 1. Thermal and structural properties of mmen-Mg_2(dobpdc).

Parameters	Value	Source
Heat capacity, kJ/(kg·K)	1.6	[102]
Sorbent density, kg/m^3	860	[103, 104]
Sorbent porosity, -	0.35	[105]
CO_2 adsorption enthalpy, kJ/mol	71	[106, 107]

The adsorption behavior of mmen-Mg_2(dobpdc) is modeled using a weighted dual-site Langmuir isotherm model, initially proposed by Hefti et al. [103] and refined by Darunte et al. [104]. The equilibrium loading is expressed as:

$$q_{\mathrm{eq}} = q_{\mathrm{low}}\left(1-w\right) + q_{\mathrm{high}}\,w \tag{7}$$

$$q_{\mathrm{low}} = \frac{q_{\mathrm{L}}\left(b_{\mathrm{L}}\,p_{\mathrm{CO_2}}\right)^{n}}{1+\left(b_{\mathrm{L}}\,p_{\mathrm{CO_2}}\right)^{n}} \tag{8}$$

$$q_{\mathrm{high}} = \frac{q_{\mathrm{H}}\,b_{\mathrm{H}}\,p_{\mathrm{CO_2}}}{1+b_{\mathrm{H}}\,p_{\mathrm{CO_2}}} + q_{\mathrm{U}}\,p_{\mathrm{CO_2}} \tag{9}$$

$$w = \exp\left(\frac{\ln\left(p_{\mathrm{CO_2}}/p_{\mathrm{step}}\right)}{\sigma}\right)\Bigg/\left(1+\exp\left(\frac{\ln\left(p_{\mathrm{CO_2}}/p_{\mathrm{step}}\right)}{\sigma}\right)\right) \tag{10}$$

where q_{low} and q_{high} quantify adsorption through two distinct mechanisms driven by differences in CO_2 partial pressure, p represents the partial pressure and w is a smoothing function used to weight these mechanisms. Temperature-dependent parameters p_{step}, b_{L}, b_{H}, q_{U}, n and σ complete the model.

The adsorption kinetics are governed by the linear driving force (LDF) model [108]:

$$\partial q/\partial t = k_{\mathrm{CO_2}}\left(q_{\mathrm{eq}} - q\right) \tag{11}$$

Integrating Eq. (11) over time yields:

$$q_{\mathrm{avg}} = q_{\mathrm{eq}}\left(1-\exp\left(-k_{\mathrm{CO_2}}\,t\right)\right) \tag{12}$$

where q_{avg} represents the average adsorption loading of the sorbent after time t, and k_{CO2} is the mass transfer constant that is determined through [108]:

$$\frac{1}{k_{\mathrm{CO_2}}} = \frac{d_{\mathrm{p}}^{2}}{60\varepsilon_{\mathrm{p}}D_{\mathrm{eff,CO_2}}} + \frac{1}{k_{\mathrm{ad,CO_2}}} \tag{13}$$

and $k_{ad,CO2}$ is the reaction kinetic parameter for intracrystalline diffusion in the micropore that is assumed to be governed by Arrhenius kinetics [108]:

$$k_{\mathrm{ad,CO_2}} = A\exp\left(\frac{\Delta E_{\mathrm{ad}}}{RT_0}\left(1-\frac{T_0}{T}\right)\right) \tag{14}$$

4.2 Carbon dioxide energy storage module

4.2.1 Compressor model

Compressors increase the pressure of gases through mechanical work input. The isentropic efficiency definition for a compressor relates the enthalpy change across the component:

$$\eta_{\mathrm{C}} = \frac{h_{\mathrm{out}}^{*} - h_{\mathrm{in}}}{h_{\mathrm{out}} - h_{\mathrm{in}}} \tag{15}$$

where h denotes the specific enthalpy, subscripts "in" and "out" indicate the inlet and outlet states, and superscript "*" denotes isentropic conditions.

The system utilizes multi-stage compression driven by off-peak grid electricity and each compression stage is usually completed by a single compressor. The electric power input of the i-th compression stage is calculated as follows:

$$\dot{W}_{\mathrm{C},i} = \dot{m}_{\mathrm{f}}\left(h_{\mathrm{out},i} - h_{\mathrm{out},i}\right) \tag{16}$$

such that the total electric power input is the sum of the power inputs of all compression stages:

$$\dot{W}_{\mathrm{C}} = \sum_{i=1}^{n_{\mathrm{C}}} \dot{W}_{\mathrm{C},i} \tag{17}$$

where $\dot{m}_{\mathrm{f}}$ represents the mass flow rate of the working fluid (WF) and n_{C} is the number of compression stages.

4.2.2 Expander model

Expanders are the functional inverse of compressors. The isentropic efficiency of an expander is:

$$\eta_{\mathrm{E}} = \frac{h_{\mathrm{in}} - h_{\mathrm{out}}}{h_{\mathrm{in}} - h_{\mathrm{out}}^{*}} \tag{18}$$

Multi-stage expansion generates electric power during peak demand periods, with each expansion stage performed by a single expander. The electric power output of the i-th expansion stage is calculated as follows:

$$\dot{W}_{\mathrm{E},i} = \dot{m}_{\mathrm{f}}\left(h_{\mathrm{in},i} - h_{\mathrm{out},i}\right) \tag{19}$$

and the total electric power output is obtained by summing the power outputs of all expansion stages n_{E}:

$$\dot{W}_{\mathrm{E}} = \sum_{i=1}^{n_{\mathrm{E}}} \dot{W}_{\mathrm{E},i} \tag{20}$$

4.2.3 Pump model

Pumps pressurize liquids and are characterized by their isentropic efficiency:

$$\eta_{\mathrm{P}} = \frac{h_{\mathrm{out}}^{*} - h_{\mathrm{in}}}{h_{\mathrm{out}} - h_{\mathrm{in}}} \tag{21}$$

Similarly, the electric power consumed by a pump is calculated as follows:

$$\dot{W}_{\mathrm{P}} = \dot{m}_{\mathrm{f}} (h_{\mathrm{out}} - h_{\mathrm{in}}) \tag{22}$$

4.2.4 Throttle valve model

Throttling processes are assumed to be fast and thus to occur at constant enthalpy:

$$h_{\mathrm{out}} = h_{\mathrm{in}} \tag{23}$$

4.2.5 HPL and LPL models

HPL and LPL storage tanks maintain thermodynamic stability according to Assumption (4):

$$P_{\mathrm{out}} = P_{\mathrm{in}} \tag{24}$$

$$T_{\mathrm{out}} = T_{\mathrm{in}} \tag{25}$$

where P and T denote pressure and temperature, respectively.

4.2.6 Heat exchanger model

Heat exchangers (i.e., intermediate coolers, reheaters and cold storage heat exchangers) satisfy energy conservation:

$$\dot{Q}_{\mathrm{HX}} = \dot{m}_{\mathrm{h}} (h_{\mathrm{h,in}} - h_{\mathrm{h,out}}) = \dot{m}_{\mathrm{c}} (h_{\mathrm{c,out}} - h_{\mathrm{c,in}}) \tag{26}$$

where subscript “HX” indicates the heat exchanger, and “h” and “c” represent the hot and cold fluid streams.

The effectiveness of a heat exchanger is defined as:

$$\varepsilon_{\mathrm{HX}} = \dot{Q}_{\mathrm{HX}} / \dot{Q}_{\max} \tag{27}$$

It is introduced to evaluate its heat transfer performance relative to an ideal heat exchanger:

$$\dot{Q}_{\max} = \left(\dot{m}c_{\mathrm{p}}\right)_{\min}\left(T_{\mathrm{h,in}} - T_{\mathrm{c,in}}\right) \tag{28}$$

where $\dot{Q}_{\max}$ is the theoretical maximum heat transfer rate, and $(\dot{m}c_{\mathrm{p}})_{\min}$ is the smaller heat-capacity rate of the hot and cold fluids when c_{p} is constant; if c_{p} varies, the theoretical maximum heat transfer rate requires pinch point analysis [95]:

$$\dot{Q}_1 = \dot{m}_{\mathrm{h}}\int_{T_{\mathrm{c,in}}}^{T_{\mathrm{h,in}}} c_{\mathrm{p,h}}dT \tag{29}$$

$$\dot{Q}_2 = \dot{m}_{\mathrm{c}}\int_{T_{\mathrm{c,in}}}^{T_{\mathrm{h,in}}} c_{\mathrm{p,c}}dT \tag{30}$$

$$\dot{Q}_3 = \dot{m}_{\mathrm{c}}\int_{T_{\mathrm{c,in}}}^{T_{\mathrm{pinch}}} c_{\mathrm{p,c}}dT + \dot{m}_{\mathrm{h}}\int_{T_{\mathrm{pinch}}}^{T_{\mathrm{h,in}}} c_{\mathrm{p,h}}dT \tag{31}$$

where T_{pinch} is the temperature at the pinch point.

The theoretical maximum heat transfer rate is the minimum of the above three parameters:

$$\dot{Q}_{\max} = \min\left(\dot{Q}_1, \dot{Q}_2, \dot{Q}_3\right) \tag{32}$$

4.3 Power-to-fuel module

4.3.1 CO_2-H_2O co-electrolysis and methanation model

The SOEC operates under three thermal modes based on the applied voltage: endothermic, exothermic and thermoneutral. With H-TES storing heat from the SOEC, it maintains exothermic operation at 1073 K.

In CO_2-H_2O co-electrolysis, the core reactions are initiated:

$$\mathrm{H_2O} \rightarrow \mathrm{H_2} + \frac{1}{2}\mathrm{O_2} \tag{33}$$

$$\mathrm{CO_2} \rightarrow \mathrm{CO} + \frac{1}{2}\mathrm{O_2} \tag{34}$$

Additionally, the RWGS reaction plays an important role in the process:

$$\mathrm{H_2} + \mathrm{CO_2} \Leftrightarrow \mathrm{H_2O} + \mathrm{CO} \tag{35}$$

The equilibrium constant of the RWGS reaction is temperature-dependent [109]:

$$\ln(K_{\mathrm{p}}) = \frac{4.92\times10^{3}}{T} - 7.78\times10^{-1}\ln(T) + 2.56\times10^{-3}T - 5.10\times10^{-7}T^{2} - 1.25 \tag{36}$$

The operating voltage combines the Nernst potentials and overpotentials:

$$E_{\mathrm{cell}} = E_{\mathrm{rev,H_2}} + \eta_{\mathrm{act}}(i_{\mathrm{H_2}}) + \eta_{\mathrm{ohm}}(i_{\mathrm{H_2}}) + \eta_{\mathrm{conc}}(i_{\mathrm{H_2}}) \tag{37}$$

$$E_{\text{cell}} = E_{\text{rev,CO}} + \eta_{\text{act}}(i_{\text{CO}}) + \eta_{\text{ohm}}(i_{\text{CO}}) + \eta_{\text{conc}}(i_{\text{CO}}) \tag{38}$$

where $E_{\text{rev,H2}}$ and $E_{\text{rev,CO}}$ are the Nernst potentials for H_2 and CO, respectively, and η_{act}, η_{ohm} and η_{conc} are the activation, ohmic and concentration overpotentials, respectively.

The Nernst potentials for H_2 and CO are given by:

$$E_{\text{rev,H}_2} = \frac{\Delta G_{\text{H}_2}}{2F} + \frac{RT}{2F}\ln\left(\frac{p^0_{\text{H}_2}(p^0_{\text{O}_2})^{0.5}}{p^0_{\text{H}_2\text{O}}}\right) \tag{39}$$

$$E_{\text{rev,CO}} = \frac{\Delta G_{\text{CO}}}{2F} + \frac{RT}{2F}\ln\left(\frac{p^0_{\text{CO}}(p^0_{\text{O}_2})^{0.5}}{p^0_{\text{CO}_2}}\right) \tag{40}$$

where F is the Faraday constant, R is the universal gas constant, and p_j^0 is the partial pressure of the species j at the electrode surface, where j denotes either H_2 or CO.

The relationship between the activation overpotential and current density can be expressed as:

$$i_{\text{H}_2} = i_{0,\text{H}_2}\left[\exp\left(\frac{(1+\kappa_{\text{a}})F\eta_{\text{c}}}{RT}\right) - \exp\left(-\frac{\kappa_{\text{c}}F\eta_{\text{c}}}{RT}\right)\right] \tag{41}$$

$$i_{\text{CO}} = i_{0,\text{CO}}\left[\exp\left(\frac{\kappa_{\text{a}}F\eta_{\text{c}}}{RT}\right) - \exp\left(-\frac{(1+\kappa_{\text{c}})F\eta_{\text{c}}}{RT}\right)\right] \tag{42}$$

$$i_j = i_{0,\text{O}_2}\left[\exp\left(\frac{\kappa_{\text{a}}F\eta_{\text{a}}}{RT}\right) - \exp\left(-\frac{\kappa_{\text{c}}F\eta_{\text{a}}}{RT}\right)\right] \tag{43}$$

where κ is the symmetry factor or charge transfer coefficient, and the ohmic overpotential is calculated considering only the electrolyte layer as follows:

$$\eta_{\text{ohm}} = R_{\text{e}} i \tag{44}$$

and R_{e} is the resistance of the electrolyte layer:

$$R_{\text{e}} = d_{\text{e}}/\sigma_{\text{e}} \tag{45}$$

Here, d_{e} is the electrolyte layer thickness, and σ_{e} is the conductivity of the layer, which depends on temperature and is given by:

$$\sigma_{\text{e}} = \frac{\sigma_0}{T}\exp\left(\frac{-E_{\text{el}}}{RT}\right) \tag{46}$$

where σ_0 is the pre-exponential factor, and E_{el} is the activation energy for ion transport [110].

The concentration overpotential depends on the partial pressure of the species at the electrode-electrolyte surface and can be expressed as:

$$\eta_{\text{conc,c}}(i_{\text{H}_2}) = \frac{RT}{2F}\ln\left(\frac{p^{\text{I}}_{\text{H}_2} p^{0}_{\text{H}_2\text{O}}}{p^{0}_{\text{H}_2} p^{\text{I}}_{\text{H}_2\text{O}}}\right) \tag{47}$$

$$\eta_{\text{conc,c}}(i_{\text{CO}}) = \frac{RT}{2F}\ln\left(\frac{p^{\text{I}}_{\text{CO}} p^{0}_{\text{CO}_2}}{p^{0}_{\text{CO}} p^{\text{I}}_{\text{CO}_2}}\right) \tag{48}$$

$$\eta_{\text{conc,a}} = \frac{RT}{2F}\ln\left[\left(\frac{p^{\text{I}}_{\text{O}_2}}{p^{0}_{\text{O}_2}}\right)^{0.5}\right] \tag{49}$$

where p_j^{I} denotes the partial pressure of the species *j* at the electrode-electrolyte surface.

The relationship between the electrolysis products and current follows Faraday's law:

$$I_j = i_j A_{\text{cell}} N_{\text{cells}} \tag{50}$$

$$\dot{N}_j = I_j / 2F \tag{51}$$

The outlet temperature of the electrolytic cell is calculated using the principle of energy conservation:

$$\sum (Mc_{\text{p}})_{\text{out}} \frac{dT_{\text{out}}}{dt} = \dot{W}_{\text{SOEC}} + \sum (\dot{m}h)_{\text{in}} - \sum (\dot{m}h)_{\text{out}} \tag{52}$$

where $\dot{W}_{\text{SOEC}}$ is the electrical power input to the electrolytic cell.

The simulated parameters for the CO_2-H_2O co-electrolysis mode are summarized in Table 2.

Table 2. CO_2-H_2O co-electrolysis simulation parameters.

Parameter	**Value**	**Source**
SOEC operating mode, -	Exothermic	[96]
SOEC inlet temperature, K	1073	[96]
Anode asymmetry factor for H_2 electrode, -	0.7	[111]
Anode asymmetry factor for CO electrode, -	0.5	[111]
Cathode asymmetry factor, -	0.1	[111]
Operating voltage, V	1.4	[96]
Active area of each cell, cm^2	100	[112]
SOEC operating pressure, MPa	1.13	[113]

The syngas (a mixture of H_2 and CO) produced by SOEC co-electrolysis, together with any unconverted CO_2, enters the methanation reactor at 523 K, where it undergoes an exothermic conversion:

$$CO + 3H_2 \rightarrow CH_4 + H_2O \qquad \Delta H = -215.4\ \text{kJ/mol (523 K)} \tag{53}$$

$$CO_2 + 4H_2 \rightarrow CH_4 + 2H_2O \qquad \Delta H = -175.8\ \text{kJ/mol (523 K)} \tag{54}$$

4.3.2 Standalone H_2O electrolysis and H_2 production model

In standalone H_2O electrolysis mode, the SOEC performs water splitting as shown in Eq. (33), producing H_2 and O_2. H_2 is used as a clean zero-carbon fuel, while O_2 is released as a by-product. The schematic of the P2F module in this mode is illustrated in Fig. 5. This process operates at 1073 K to maximize ionic conductivity and catalytic activity. The thermal and electrochemical parameters for this mode mirror those of the CO_2-H_2O co-electrolysis mode.

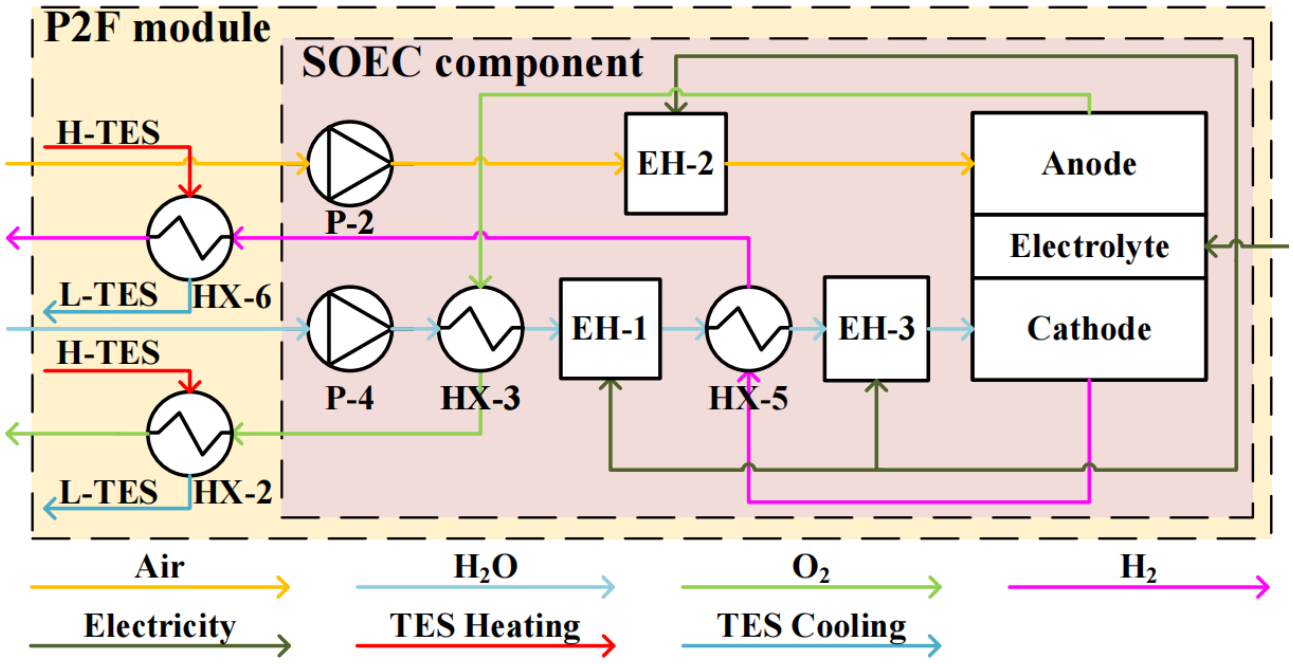


Fig. 4. Schematic diagram of the P2F module in standalone H_2O electrolysis mode.

4.4 Exergy analysis

Under Assumption (3), the exergy within the system is categorized into physical and chemical components. The total exergy for each stream is expressed as:

$$\dot{E}x = \dot{m}_f ex = \dot{m}_f \left(ex_{ph} + ex_{ch} \right) \tag{55}$$

Physical exergy and chemical exergy are calculated as follows:

$$ex_{ph} = \left(h - h_0 \right) - T_0 \left(s - s_0 \right) \tag{56}$$

$$ex_{ch} = \sum_{j=1}^{N} z_j ex_j^{ch} + RT_0 \left(\sum_{j=1}^{N} z_j \ln\left(z_j \right) \right) \tag{57}$$

where z_j denotes the mole fraction of species j and ex_j^{ch} denotes the standard chemical exergy of species j [114].

4.5 Economic analysis

The Chemical Engineering Plant Cost Index (CEPCI) is adopted in this study to adjust all capital cost estimates to a consistent reference year. As a widely used index in the chemical and energy industries, the CEPCI reflects changes in construction costs, equipment prices and labor rates over time, enabling a more accurate and up-to-date economic analysis. All capital costs in this study are adjusted to the year of 2023 using CEPCI values [59]:

$$Z_{2023}/Z_{\text{refer}} = CEPCI_{2023}/CEPCI_{\text{refer}} \tag{58}$$

where Z represents the purchased cost of the component, and the subscript "refer" denotes the reference year. Table 3 summarizes the purchase costs of the components in the system.

Table 3. Component investment cost.

Component	Cost equation/$
Heat exchanger [115]	$Z_{HX} = 12000 \times (A_{HX} / 100)^{0.6}$
Compressor [116]	$Z_C = 71.1 \times \dot{m}_i / (0.92\text{-}\eta_C) \times \pi_C \times \ln(\pi_C)$
Expander [116]	$Z_E = 479.34 \times \dot{m}_i / (0.93\text{-}\eta_E) \times \ln(\pi_E) \times [1 + \exp(0.036 \times T_i - 54.4)]$
Vacuum pump [108]	$Z_{VP} = 19123.137 + 278.58745 \times (\dot{Q})^{0.61845}$
Pump [117]	$Z_P = 200 \times (\dot{W})^{0.65}$
Condenser [118]	$Z_{CON} = 8000 \times (A_{CON} / 100)^{0.6}$
Cold box [119]	$Z_{CB} = 32.8 \times (A_{CB} / 80)^{0.68}$
Adsorption bed [108]	$Z_{AB} = 50 \times m_{sorbent} + F_M \times \exp[5.6336 + 0.4599 \times \ln(2.2 \times m_{reactor}) + 0.00582 \times \ln(2.2 \times m_{reactor})^2]$
Stack [120]	$Z_{STACK} = A_a \times N_{cell} \times (2.96 \times T_{SOEC} - 1907) \times (N_{system} / N_{STACK})$
Mixer [120]	$Z_{MIXER} = 0$
Storage tank [121]	$Z_{ST} = 1.218 \times F_M \times \exp[11.662 - 0.6104 \times \ln(264.17 \times V) + 0.04536 \times \ln(264.17 \times V)^2]$
Methanation reactor [122]	$Z_{MR} = 504 \times HHV_{fuel}$
Throttle valve [123]	$Z_{TV} = 114.5 \times \dot{m}$
Electrical heater [124]	$Z_{EH} = 14 \times (\dot{W})$

Component	Cost equation/$
Blower [121]	$Z_{BL} = 1.218 \times F_M \times F_P \times \exp[0.04 + 0.1821 \times \ln(1.7896 \times \dot{m}) + 0.0786 \times \ln(1.7896 \times \dot{m})^2]$

To evaluate the economic performance of the polygeneration system, the *LCOE* is adopted to represent the cost of electricity over the system lifetime [12]:

$$LCOE = \frac{\sum Z_k + \sum_{i=1}^{N_{system}} \frac{C_{OM} + C_C}{(1+r)^i}}{\sum_{i=1}^{N_{system}} \frac{365 \times \int_0^{t_{dis}} \left(\dot{W}_{ele} + \dot{Q}_{heat}/COP_h + \dot{Q}_{cool}/COP_c + \dot{W}_{fuel}\eta_{GTC}\right)}{(1+r)^i}} \tag{59}$$

where C_{OM} is the combined operation and maintenance costs, C_C is the charging cost, r is the discount rate, and N_{system} is the operating lifetime of the system, which is set to 30 years in this study. $\dot{W}_{ele}$, $\dot{Q}_{heat}$, $\dot{Q}_{cool}$ and $\dot{W}_{fuel}$ are the electricity, heating, cooling and fuel output rates of the system, respectively.

In the above equation, the heating, cooling and fuel outputs are converted into equivalent electricity to enable a consistent comparison. Specifically, heating and cooling are converted using the coefficient of performance of a reversible heat pump operating in heating (COP_h) or cooling (COP_c) mode [57], while fuel is converted based on the assumed electricity generation efficiency of a gas turbine cycle (η_{GTC}) [125].

4.6 System parameters and metrics

4.6.1 Designed parameters

CO_2 serves as a multi-functional medium in the system, acting as a carbon capture product, energy storage medium and fuel feedstock. Fig. 6 illustrates the CO_2 mass flow distribution network within the system.

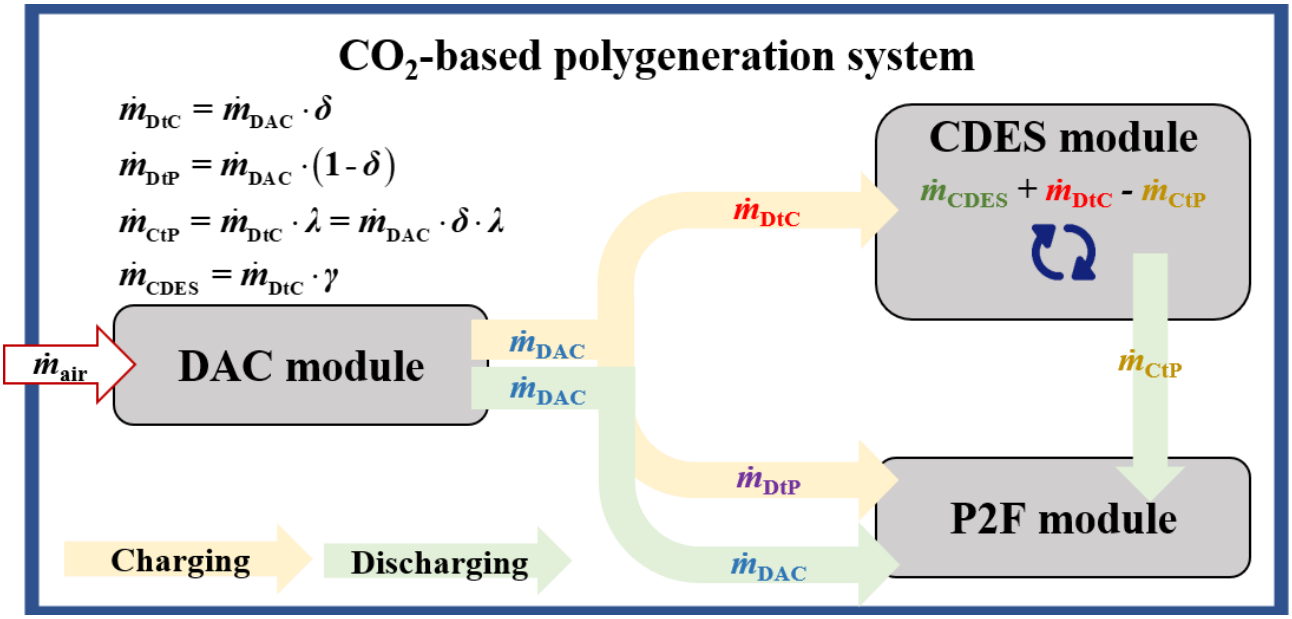


Fig. 5. CO_2 mass flow allocation schematic diagram.

To characterize the CO_2 exchange dynamics between modules, three key parameters are introduced: CO_2 primary distribution coefficient (δ), CO_2 mass flow ratio between CDES and DAC (γ) and CO_2 secondary distribution coefficient (λ). The CO_2 primary distribution coefficient (δ) governs the allocation of CO_2 mass flow from the DAC module to the CDES and P2F modules and is defined as the ratio of the CO_2 mass flow rate entering the CDES module to that at the DAC module outlet during charging:

$$\delta = \dot{m}_{\mathrm{DtC}} / \dot{m}_{\mathrm{DAC}} \tag{60}$$

The CO_2 mass flow ratio between CDES and DAC (γ) represents the scale ratio between the CDES and DAC modules:

$$\gamma = \dot{m}_{\mathrm{CDES}} / \dot{m}_{\mathrm{DAC}} \tag{61}$$

and the CO_2 secondary distribution coefficient (λ) governs the allocation of CO_2 mass flow between the CDES and P2F modules during discharging:

$$\lambda = \dot{m}_{\mathrm{CtP}} / \dot{m}_{\mathrm{DtC}} \tag{62}$$

In the above relations, $\dot{m}_{\mathrm{DAC}}$, $\dot{m}_{\mathrm{DtC}}$, $\dot{m}_{\mathrm{DtP}}$, $\dot{m}_{\mathrm{CtP,}}$ and $\dot{m}_{\mathrm{CDES}}$ are the CO_2 mass flow rates at the DAC module outlet, from the DAC module to the CDES module during charging, from the DAC module to the P2F module during charging, from the CDES module to the P2F module during discharging, and within the CDES module, respectively.

In this system, H-TES serves as a thermal hub that integrates both internal module heat and external waste heat to reheat CO_2 at the expander inlets. The heat source coefficient is defined as the ratio of the external waste heat input rate to the internal heat storage rate and is used to quantify the impact of external waste heat on system performance:

$$\alpha = \dot{Q}_{\mathrm{ext}} / \dot{Q}_{\mathrm{H\text{-}TES}} \tag{63}$$

where $\dot{Q}_{\mathrm{ext}}$ is the external waste heat input rate and $\dot{Q}_{\mathrm{H\text{-}TES}}$ is the internal heat storage rate in the H-TES.

The heat stored in the H-TES serves two purposes: one part is used for reheating CO_2 at the expander inlets, while the rest is supplied externally. The heat allocation ratio is defined as the ratio of the mass flow rate of the heat transfer fluid (HTF) used for CO_2 reheating to the total HTF mass flow rate in the H-TES and is used to clarify heat distribution within the system:

$$\zeta = \dot{m}_{\mathrm{HTF,pre}} / \dot{m}_{\mathrm{HTF,tot}} \tag{64}$$

where $\dot{m}_{\mathrm{HTF,pre}}$ and $\dot{m}_{\mathrm{HTF,tot}}$ are the HTF mass flow rates used for CO_2 reheating at the expander inlets and in the H-TES overall, respectively.

4.6.2 Performance metrics

The total electrical output rate of the system is derived solely from the expander:

$$\dot{W}_{\mathrm{ele}} = \dot{W}_{\mathrm{E}} \tag{65}$$

The heating and cooling output rates are derived from the corresponding enthalpy differences:

$$\dot{Q}_{\mathrm{heat}} = \dot{m}_{\mathrm{h,f}} (h_{\mathrm{h,f}} - h_{\mathrm{h,f,0}}) \tag{66}$$

$$\dot{Q}_{\mathrm{cool}} = \dot{m}_{\mathrm{c,f}} (h_{\mathrm{c,f,0}} - h_{\mathrm{c,f}}) \tag{67}$$

where $\dot{m}_{\mathrm{h,f}}$ and $\dot{m}_{\mathrm{c,f}}$ are the mass flow rates of the hot and cold WFs, respectively, $h_{\mathrm{h,f}}$ and $h_{\mathrm{c,f}}$ represent the specific enthalpies of the hot and cold WFs at the H-TES and L-CES temperatures, and subscript "0" represents the ambient temperature.

The fuel output rate of the system is the product of the CH_4 mass flow rate and its lower heating value (*LHV*):

$$\dot{Q}_{\mathrm{fuel}} = \dot{m}_{\mathrm{CH_4}} LHV_{\mathrm{CH_4}} \tag{68}$$

The system energy utilization factor (*EUF*) accounts for all output forms [126]:

$$EUF = \frac{\int_0^{t_{\mathrm{dis}}} \dot{W}_{\mathrm{ele}} + \dot{Q}_{\mathrm{heat}} + \dot{Q}_{\mathrm{cool}} + \dot{Q}_{\mathrm{fuel}}}{\int_0^{t_{\mathrm{char}}} \dot{W}_{\mathrm{in}} + \int_0^{t_{\mathrm{dis}}} \dot{W}_{\mathrm{in}}} \tag{69}$$

where t_{dis} and t_{char} represent the discharging time and charging time, respectively, and $\dot{W}_{\mathrm{in}}$ is the electrical input rate. During discharging, the electrical output can be provided by the expander.

It should be noted that the *EUF*, as defined in this study, is based on the first law of thermodynamics and is calculated as the ratio of the total useful energy outputs (electricity, heating, cooling and fuel) to the external electricity input. Since the energy outputs include heating and cooling, and their calculation does not consider quality (as in exergy), the *EUF* can exceed 100% without violating thermodynamic laws. For example, when electricity is converted to cooling via absorption refrigeration or to heating via resistive or compression-based methods, the amount of useful thermal or cold energy delivered can numerically exceed the input electricity, resulting in a *COP* > 1. This effect contributes to the *EUF* exceeding 100%, which is acceptable under energy-based analysis.

The individual energy utilization factors are defined for the four energy forms delivered by the system: electricity, heating, cooling and fuel:

$$EUF_{\text{type}} = \int_0^{t_{\text{dis}}} \dot{W}_{\text{type}} \Bigg/ \left(\int_0^{t_{\text{char}}} \dot{W}_{\text{in}} + \int_0^{t_{\text{dis}}} \dot{W}_{\text{in}} \right) \text{ or } \int_0^{t_{\text{dis}}} \dot{Q}_{\text{type}} \Bigg/ \left(\int_0^{t_{\text{char}}} \dot{W}_{\text{in}} + \int_0^{t_{\text{dis}}} \dot{W}_{\text{in}} \right) \tag{70}$$

where "type" denotes the energy form (ele/heat/cool/fuel).

Thermal exergy contributions from heating and cooling processes are expressed as:

$$\dot{E}x_{\text{heat}} = \dot{Q}_{\text{heat}} (1 - T_0/T) \tag{71}$$

$$\dot{E}x_{\text{cool}} = \dot{Q}_{\text{cool}} (1 - T/T_0) \tag{72}$$

where T_0 is the reference temperature.

The system exergy utilization factor (*ExUF*) reflects the quality of energy conversion:

$$ExUF = \frac{\int_0^{t_{\text{dis}}} \dot{W}_{\text{ele}} + \dot{E}x_{\text{heat}} + \dot{E}x_{\text{cool}} + \dot{E}x_{\text{fuel}}}{\int_0^{t_{\text{char}}} \dot{W}_{\text{in}} + \int_0^{t_{\text{dis}}} \dot{W}_{\text{in}}} \tag{73}$$

The discharging power ratio is given by:

$$\beta = \dot{W}_{\text{dis,ele,out}} \Big/ \dot{W}_{\text{dis,ele,in}} \tag{74}$$

where $\dot{W}_{\text{dis,ele,out}}$ and $\dot{W}_{\text{dis,ele,in}}$ are the electrical output and input rates during the discharging process, respectively. A ratio exceeding 100% indicates surplus electricity, enabling net export to the grid.

5. Results and discussion

This section presents a comprehensive parametric analysis of the system, followed by the constrained optimization of the key parameters. Table 4 summarizes the design values for all parameters, with nontarget parameters fixed at their specified design values for subsequent analyses.

Table 4. System parameters under design conditions.

Parameter	Value
CO_2 mass flow rate at DAC outlet, kg/s	1.45×10^{-1}
CO_2 primary distribution coefficient, -	0.5
CO_2 secondary distribution coefficient, -	1
CO_2 mass flow ratio between CDES and DAC, -	500
Adsorption temperature, K	303
Desorption temperature, K	363

Parameter	Value
Compression and expansion stage numbers, -	(2, 2)
H-TES heat allocation ratio, %	94
Heat source coefficient, -	-
External waste heat temperature, K	-
SOEC operating mode, -	CO_2-H_2O co-electrolysis
SOEC operating pressure, MPa	1.13
SOEC charging/discharging operating voltage, V	1.4
Lifetime of the SOEC stack, yr	7.5 [97, 127]
Lifetime of the system, yr	30

5.1 Influence of CO_2 flow parameters

5.1.1 CO_2 mass flow rate at the DAC outlet

The CO_2 mass flow rate at the DAC outlet is a key scaling parameter for the system, directly influencing the energy input and output rates. As shown in Fig. 7, the system is insensitive to the CO_2 flow rate across a range spanning three orders of magnitude (1.45×10^{-4} to 1.45 kg/s). The energy utilization factor (80%), exergy utilization factor (57%) and discharging power ratio (152%) remain stable, highlighting the scalability of the system.

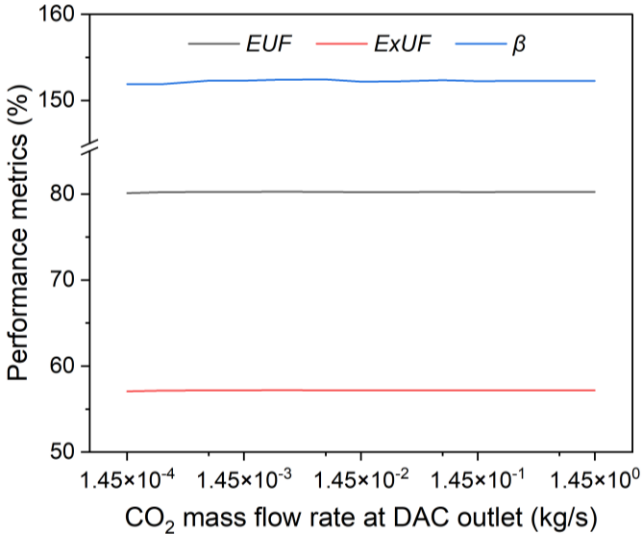


Fig. 6. Effect of the CO_2 mass flow rate at the DAC outlet on system performance metrics.

5.1.2 CO_2 flow allocation dynamics between DAC and CDES

The CO_2 flow allocation between DAC and CDES is influenced by two key parameters: the CO_2 primary distribution coefficient (δ) and the CO_2 mass flow ratio between CDES and DAC (γ). Fig. 8 demonstrates

that while δ has little impact on the individual energy utilization factors, γ significantly influences system behavior.

Fig. 8 (a) and (b) demonstrate the variations in the electricity and heating utilization factors. As γ increases, the resulting increase in the CO_2 mass flow rate within the CDES module during internal circulation leads to higher electricity demands and greater generation of compression heat and expansion work. Since the CDES module's electricity and heating outputs dominate those of the other two modules, this leads to corresponding increases in the electricity and heating utilization factors. Fig. 8 (c) shows that the cooling utilization factor remains consistently at zero due to the system's inherent inability to generate cold energy in this configuration. Fig. 8 (d) demonstrates the decrease in the fuel utilization factor with increasing γ, which stems from the higher total energy input required by the system. Since the fuel output remains constant, this elevated energy demand inevitably reduces the fuel utilization factor.

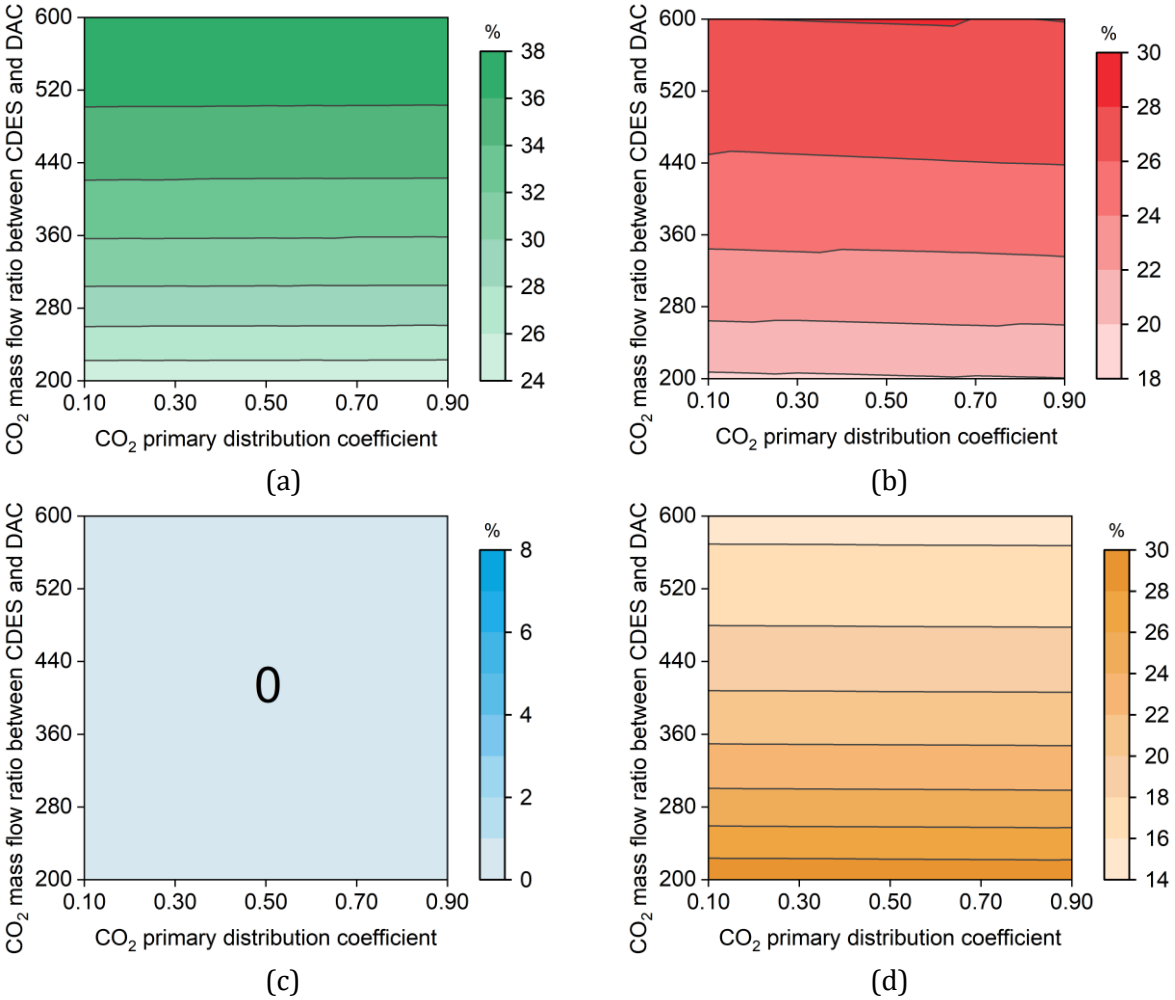


Fig. 7. Effect of the CO_2 primary distribution coefficient (δ) and the CO_2 mass flow ratio between CDES and DAC (γ) on: (a) electricity utilization factor, EUF_{ele}, (b) heating utilization factor, EUF_{heat}, (c) cooling utilization factor, EUF_{cool} and (d) fuel utilization factor, EUF_{fuel}.

Fig. 9 shows the effect of the CO_2 primary distribution coefficient (δ) and the CO_2 mass flow ratio between CDES and DAC (γ) on the system performance metrics, with δ also having a negligible influence.

Fig. 9 (a) and (b) show that increasing γ improves the system's energy and exergy utilization factors. This is due to the system's ability to generate more electricity and thermal energy as γ rises, as seen in Fig. 8 (a) and (b). Although the fuel utilization factor declines with higher γ, this is offset by significant gains in electricity and heating outputs, resulting in a net improvement in energy and exergy utilization. Specifically, as γ increases from 200 to 600, the system energy and exergy utilization factors increase by 7.9% and 3%, respectively.

Fig. 9 (c) illustrates the combined effect of δ and γ on the discharging power ratio. Increasing γ boosts the stored CO_2 mass in the CDES, enhancing expansion work during discharging. Simultaneously, a lower δ reduces the CO_2 flow into the CDES during charging, decreasing the electrolyzer's CO_2 processing load for discharging. Together, these factors increase the discharging power ratio. Specifically, a 100-unit increase in γ improves discharging autonomy by approximately 30%, whereas decreasing δ from 0.7 to 0.3 raises β by 20%. This interplay of γ and δ optimizes electricity export capacity and operational flexibility.

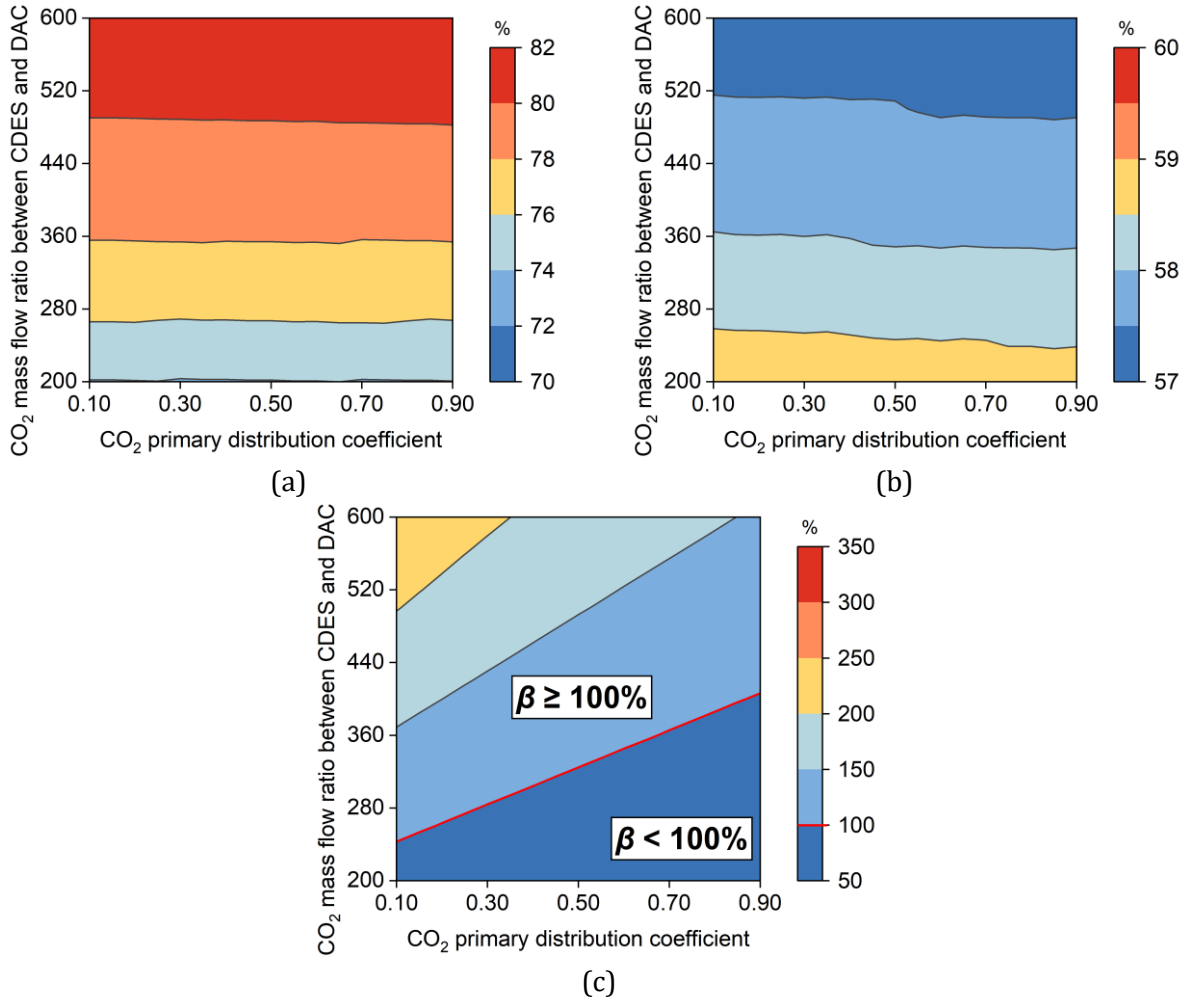
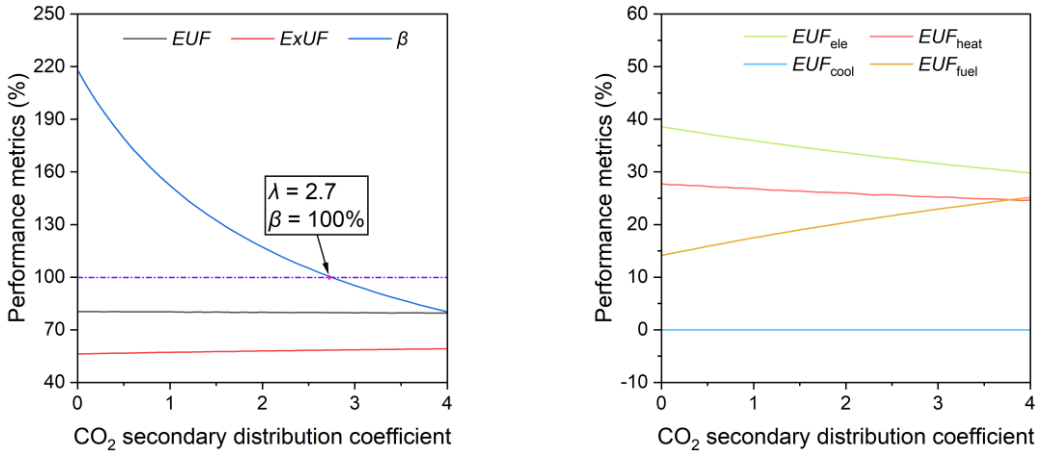


Fig. 8. Effect of the CO_2 primary distribution coefficient (δ) and the CO_2 mass flow ratio between CDES and DAC (γ) on: (a) system energy utilization factor, *EUF*, (b) system exergy utilization factor, *ExUF* and (c) discharging power ratio, β.

5.1.3 CO_2 secondary distribution coefficient

Fig. 10 shows the impact of the CO_2 secondary distribution coefficient (λ) on the system and individual performance metrics, focusing on the discharging power ratio and the electrical and fuel utilization factors.

Fig. 10 (a) illustrates that as λ increases from 0 to 4, the discharging power ratio drops from 218% to 80%, crossing the self-sufficiency threshold (β = 100%) at λ = 2.7. System energy and exergy utilization factors remain nearly unchanged. Fig. 10 (b) shows that higher λ values increase electricity consumption for co-electrolysis, raising fuel energy utilization (EUF_{fuel} from 14% to 25%) but decreasing exportable electricity (EUF_{ele} from 38% to 30%). λ becomes a key control parameter, with the system operating in net electricity export mode (β > 100%) when λ < 2.7. Beyond this point, grid support is required. Strategic λ modulation enables dynamic output configuration, balancing electricity generation with fuel synthesis while maintaining operational flexibility for grid interaction and multi-energy dispatch. The CO_2 not entering the P2F module is directed through HX-1, where its waste heat is stored in the H-TES. Increasing λ reduces CO_2 flow to HX-1, lowering heating output (EUF_{heat} from 28% to 25%), but λ has no effect on the cooling utilization factor (EUF_{cool}).



(a) (b)

Fig. 9. Effect of the CO_2 secondary distribution coefficient on: (a) system performance metrics and (b) individual energy utilization factors.

5.2 Effect of adsorption and desorption temperatures in the DAC module

The adsorption temperature (T_{ads}) governs the equilibrium CO_2 loading of the mmen-Mg_2(dobpdc) sorbent (Eqs. (7)-(10)). For a constant CO_2 capture rate, there is an inverse correlation between equilibrium CO_2 loading and sorbent mass. Changes in T_{ads} affect the total sorbent mass and the thermal demand during desorption (Eq. (3)). Additionally, Eqs. (3) and (4) show that the desorption temperature (T_{des}) governs the thermal requirements for regeneration. Thus, T_{ads} and T_{des} in the DAC module significantly impact system performance via thermal energy demands.

Fig. 11 illustrates the effects of T_{ads} and T_{des} on the system energy and exergy utilization factors. As shown in Fig. 11 (a) and (b), for a CO_2 concentration of 400 ppm, when T_{ads} exceeds 313 K, the sorbent's CO_2

loading capacity decreases sharply, leading to the need for a greater sorbent mass and higher heat demand during desorption. This exceeds the available thermal energy, reducing both system utilization factors. When T_{ads} is below 310 K, T_{des} has minimal impact on performance. However, above this threshold, higher T_{des} significantly increases the energy demand for desorption, worsening the energy and exergy utilization factors. These results highlight the importance of maintaining T_{ads} below 313 K to optimize system performance.

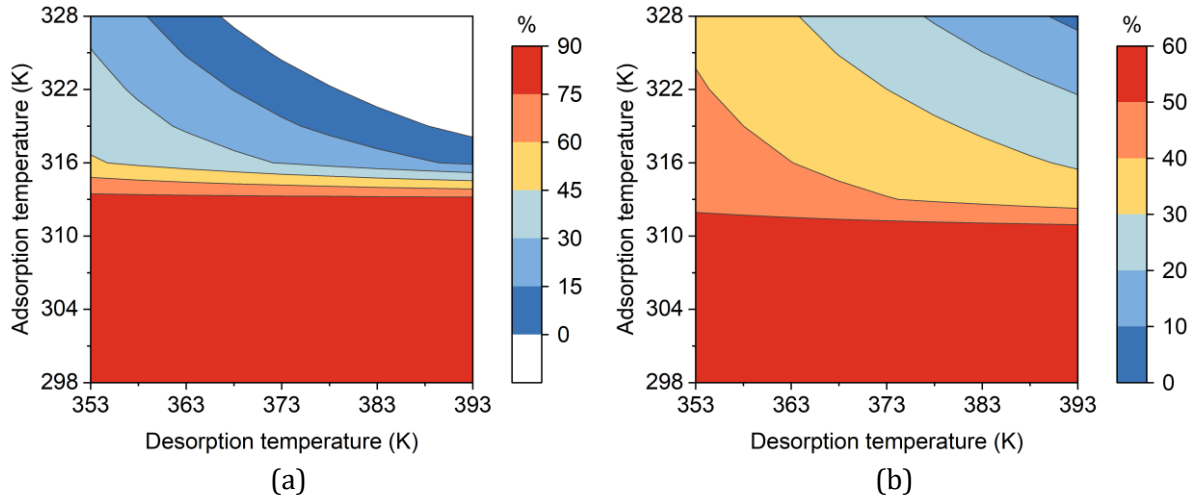


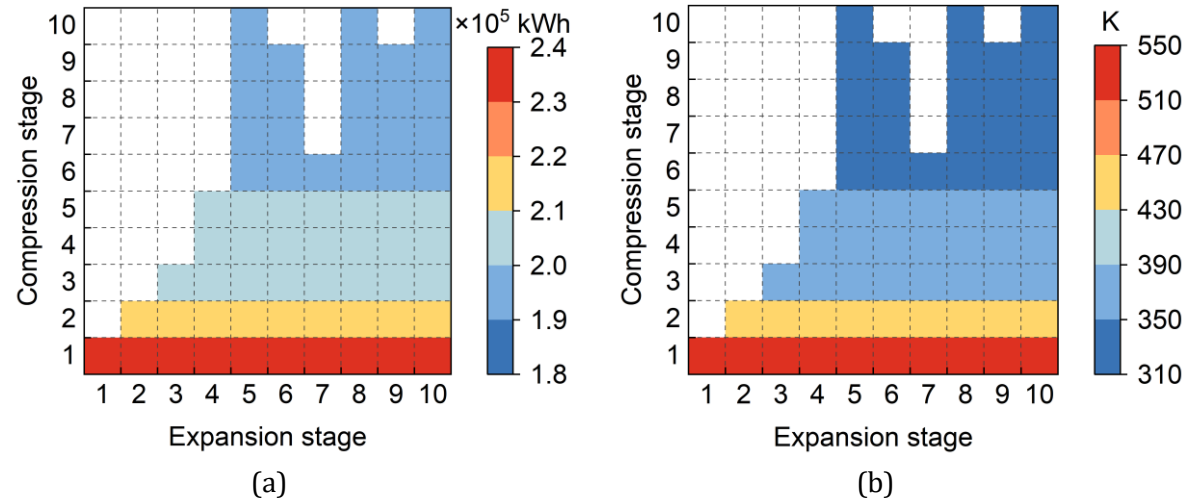
Fig. 10. Effect of the adsorption and desorption temperatures on: (a) system energy utilization factor, *EUF* and (b) system exergy utilization factor, *ExUF*.

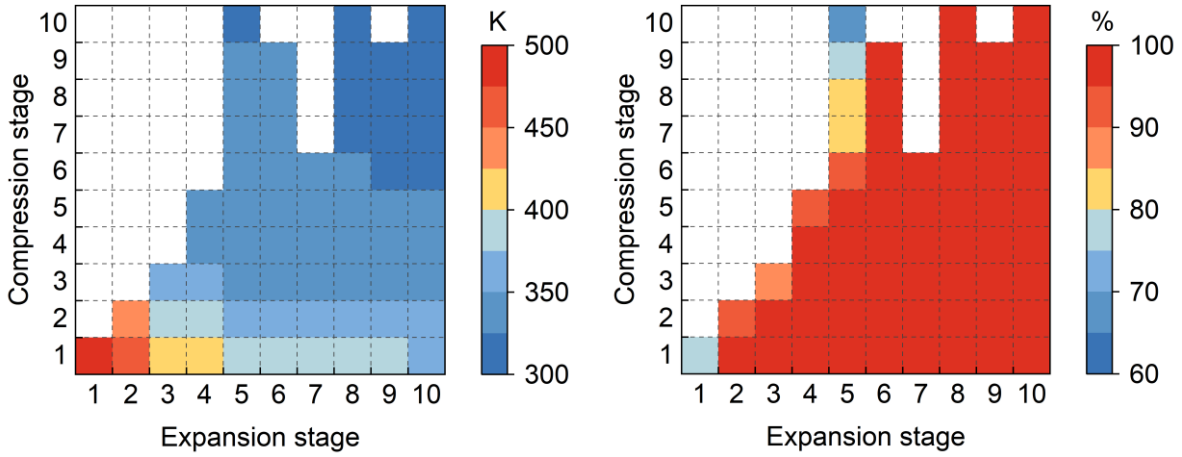
5.3 Effect of compression and expansion stage numbers in the CDES module

The feasible numbers of compression and expansion stages are identified by ensuring that CO_2 remains in the gaseous or supercritical phase at all expander outlets, thereby avoiding phase change. Only these thermodynamically stable configurations are considered in further analysis, excluding those prone to two-phase flow or liquid formation, which would degrade system performance metrics.

5.3.1 H-TES performance metric

Fig. 12 illustrates the impact of compression and expansion stage configurations on the H-TES performance metrics.





(c) (d)

Fig. 11. Effect of the compression and expansion stage numbers on: (a) stored thermal energy, (b) temperature profile, (c) maximum expander inlet temperature and (d) maximum heat allocation ratio.

As shown in Fig. 12 (a) and (b), the thermal energy storage capacity and temperature of the H-TES are primarily determined by the number of compression stages (n_c), with the number of expansion stages having no measurable effect. Increasing nc from one to ten reduces the stored heat by 18% and lowers the temperature by 38%, with these trends being consistent across all expansion stage configurations.

Fig. 12 (c) shows the maximum expander inlet temperature. For a fixed n_c, increasing the number of expansion stages results in the thermal energy being distributed across more stages. This leads to a proportional reduction in the heat allocation per reheater, lowering the maximum CO_2 inlet temperature at the expander.

Fig. 12 (d) demonstrates configuration-dependent variations in the maximum heat allocation ratio (ζ). The (1, 1) configuration achieves ζ = 75% and is constrained by inefficient heat exchange caused by excessive temperature gradients during CO_2 reheating from the high-temperature TES. Conversely, the (10, 5) configuration utilizes sub-ambient CO_2 temperatures after the third to fifth expansion stages for cold storage, which reduces reheating demands and lowers ζ to 67%.

5.3.2 Individual energy utilization factor

Fig. 13 illustrates the relationship between the compression and expansion stage configuration and the individual energy utilization factors

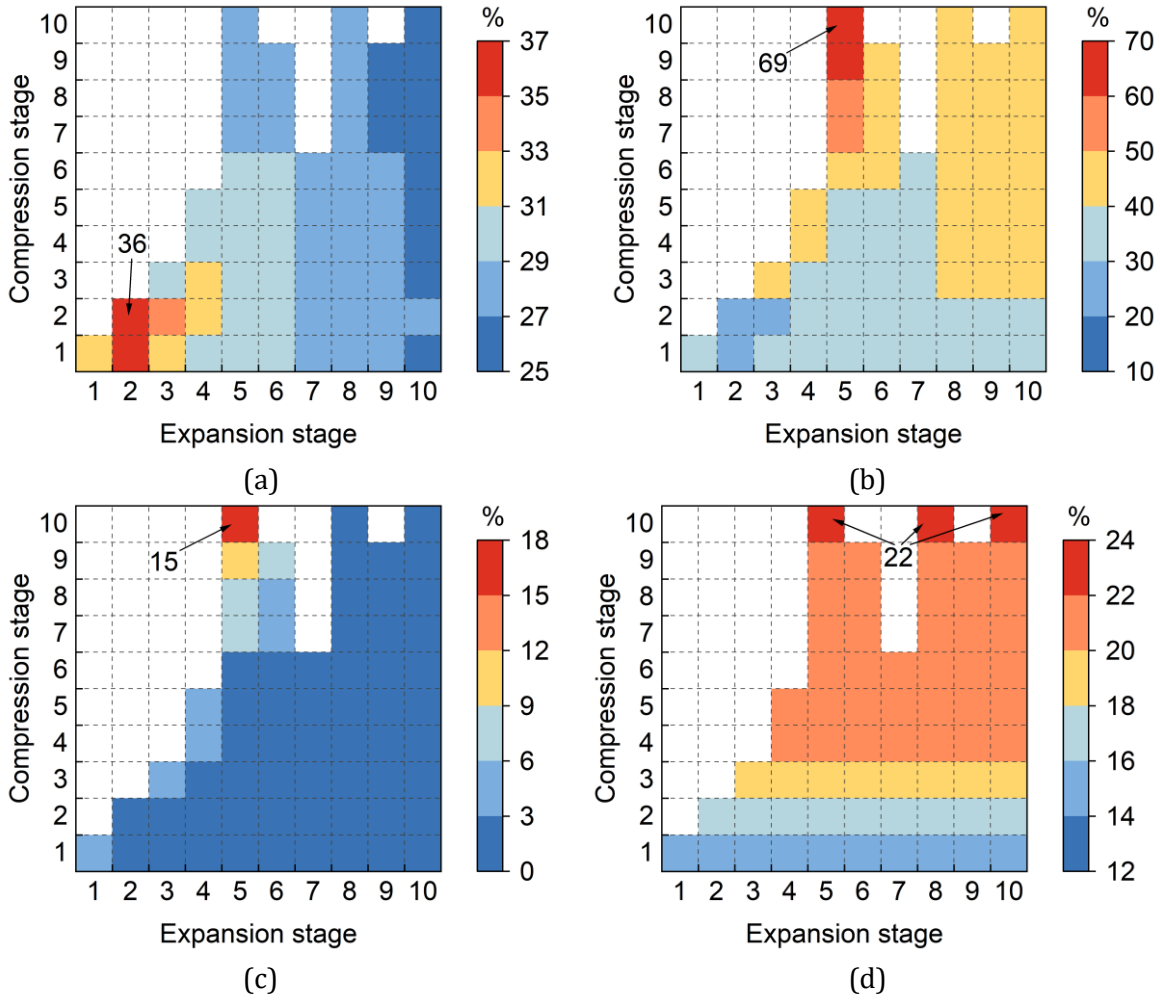


Fig. 12. Effect of the compression-and-expansion stage configuration on: (a) electricity utilization factor, EUF_{ele}, (b) heating utilization factor, EUF_{heat}, (c) cooling utilization factor, EUF_{cool} and (d) fuel utilization factor, EUF_{fuel}.

Fig. 13 (a) shows that the electricity utilization factor ranges from 26% to 36%. The optimal value (36%) occurs at the (2, 2) stage configuration, which strikes a balance between compression work reduction and thermal energy availability. A single expansion stage configuration is limited by the heat exchanger effectiveness, with a maximum H-TES allocation ratio of 75% (see Fig. 12 (d)) for CO_2 heating. In contrast, multi-expansion stage systems (with one or two compression stages) exhibit a significantly improved H-TES allocation ratio, but beyond a single expansion stage, the distribution of thermal energy across additional reheaters leads to a decrease in the electricity utilization factor. The optimal configuration for electrical utilization is the (2, 2) configuration, which maximizes heat-to-electricity conversion efficiency while mitigating entropy effects.

Fig. 13 (b) and (c) highlight the heating (69%) and cooling (15%) utilization factors, both of which reach their optimal values under the (10, 5) configuration. As the number of expansion stages exceeds three, increasing the number of compression stages improves both the heating and cooling utilization factors. This trend is most pronounced when the number of expansion stages is five. In multi-stage expansion systems, cold energy recovery from downstream expanders reduces the thermal energy required for CO_2

reheating, lowering the total heat consumption and allowing for the simultaneous optimization of both the heating and cooling utilization factors.

The co-electrolysis process maintains a constant fuel output independent of compression and expansion stage configurations. In Fig. 13 (d), fuel utilization factor variations (15-22%) are exclusively governed by the system energy input: multi-stage compression reduces energy consumption, achieving a maximum fuel utilization factor of 22% at ten compression stages.

5.3.3 System performance metrics

Fig. 14 shows the effect of the compression and expansion stage numbers on the system energy and exergy utilization factors. Fig. 14 (a) demonstrates that the (10, 5) compression and expansion configuration achieves the highest system energy utilization factor of 134%. With total energy input and output of 1.38×10^5 kWh and 1.84×10^5 kWh, the configuration results in electricity (27%), heating (69%), cooling (15%) and fuel (22%) utilization factors. When the number of expansion stages (n_E) is ≤ 6, increasing the number of compression stages (n_C) reduces electricity demand during charging, which lowers the H-TES storage temperature and consequently decreases the expander inlet temperature, triggering cold energy production. This dual effect provides cooling output and reduces internal thermal energy demand, leading to an increased system energy utilization factor. This synergy is discussed in Section 5.3.2.

Fig. 14 (b) shows that the system exergy utilization factor improves with increasing n_C and decreasing n_E, peaking at 60% for the (1, 1) configuration. The (10, 5) configuration achieves an exergy utilization factor of 58%, which is 2 percentage points lower than the peak value. This minimal reduction highlights the configuration's ability to effectively balance a high energy utilization factor with the utilization of multiple energy forms, despite prioritizing energy quantity over absolute exergy preservation.

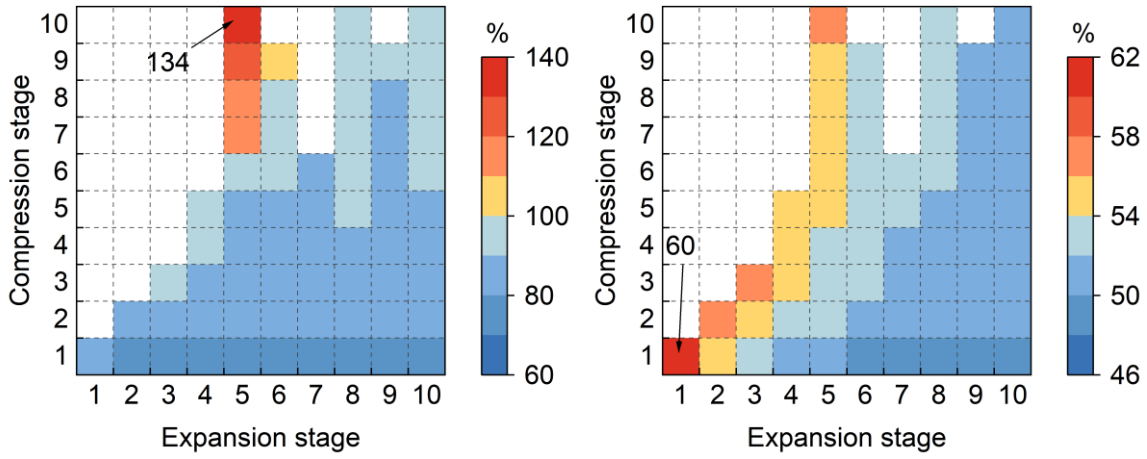


Fig. 13. Effect of the compression and expansion stage numbers on: (a) system energy utilization factor, *EUF*, and (b) system exergy utilization factor, *ExUF*.

5.4 Effect of H-TES heat allocation ratio in the CDES module

Fig. 15 shows the impact of the H-TES heat allocation ratio (ζ) on the system performance within the

constrained range from 80% to 96%. The upper limit (96%) is constrained by the heat exchanger effectiveness, while the lower limit (80%) prevents CO_2 from entering two-phase flow.

Fig. 15 (a) demonstrates that increasing ζ from 80% to 96% causes a non-monotonic variation in the system exergy utilization factor, which initially drops from 58% to 57% before slightly recovering, though it does not surpass its initial value. This change leads to a 6% reduction in the system energy utilization factor, while the discharging power ratio improves by 15%. Fig. 15 (b) reveals that higher ζ values prioritize thermal energy for CO_2 reheating at the expander inlets, enhancing electricity output (which is reflected in the discharging power ratio) but reducing heating and cooling outputs, with fuel output remaining unchanged.

When ζ is below 86%, the system maintains cooling output, which progressively decreases with increasing ζ. This reduction in cooling capacity primarily drives the observed decrease in the system exergy utilization factor. Conversely, when ζ exceeds 86%, the system converts thermal energy into electrical energy, resulting in a modest recovery of the system exergy utilization factor. The overall trend indicates that higher ζ values promote the conversion of both thermal energy and cold energy into electrical output. However, due to inherent energy losses during these conversion processes, the system energy utilization factor exhibits a consistent downward trend. This thermal allocation enables modulation of the power-to-heat ratio through ζ adjustment, where a lower ζ allows simultaneous extraction of cold energy.

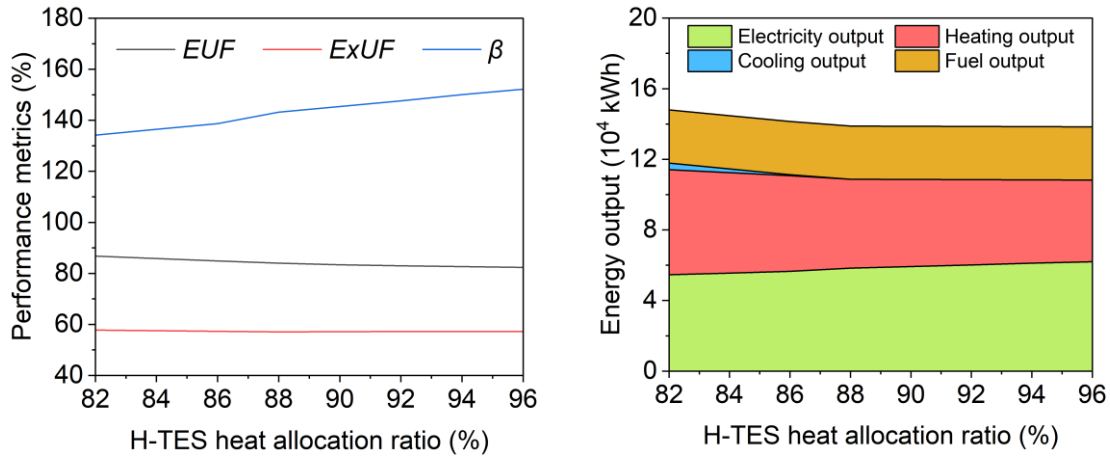


Fig. 14. Effect of the H-TES heat allocation ratio on: (a) system performance metrics and (b) energy output composition.

5.5 Effect of SOEC operating conditions in the P2F module

5.5.1 SOEC operating mode

The system primarily operates in CO_2-H_2O co-electrolysis mode for methane (CH_4) production. To accommodate regional hydrogen (H_2) demand, it switches to H_2O electrolysis mode by feeding only water and air into the SOEC, which enables hydrogen generation. Both modes use the same total H_2O input for the electrolysis process, with an H_2O conversion rate of 75% during charging and discharging.

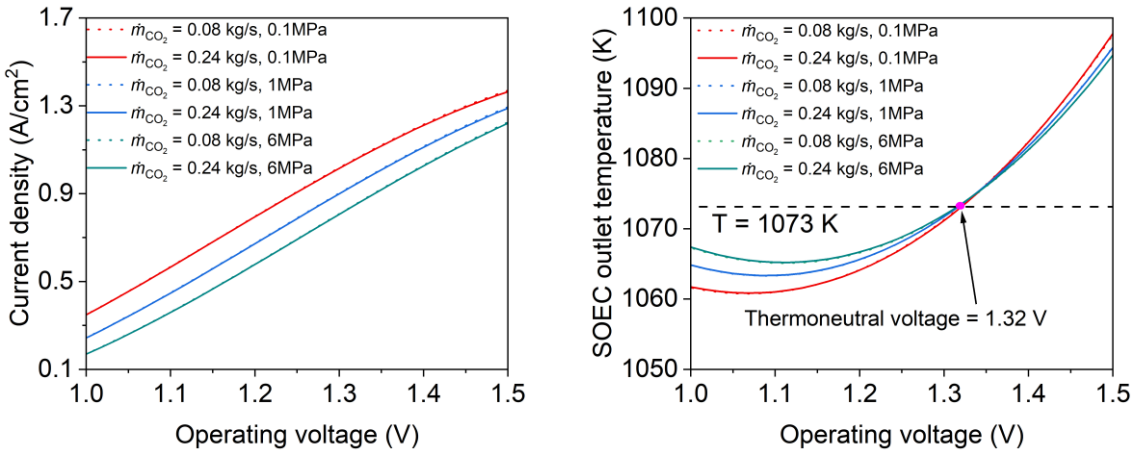
Table 5 compares the performance metrics between CO_2-H_2O co-electrolysis and H_2O electrolysis modes. H_2O electrolysis mode shows a 17% improvement in the discharging power ratio and enhances electricity dispatch flexibility. This increase enables dual utilization: direct supply or recirculation for electrolysis-driven fuel storage, with only minor changes in the core performance metrics (*EUF* = 80-81%, *ExUF* = 57-58%).

Table 5. System performance comparison between the operational modes.

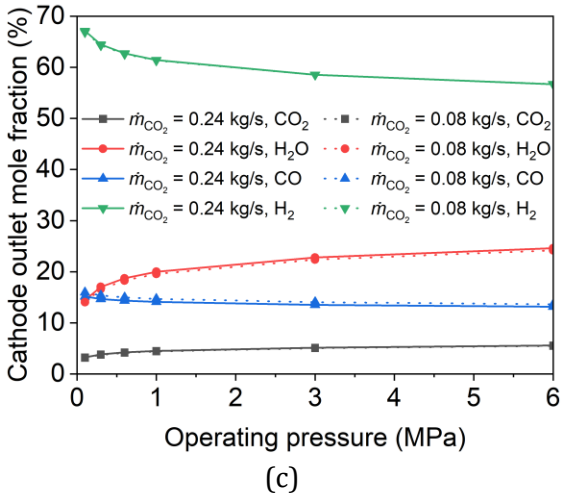
System metrics	***CO_2-H_2O co-electrolysis***	***H_2O electrolysis***
β, %	152	178
EUF, %	80	81
ExUF, %	57	58
EUF_{ele}, %	36	37
EUF_{heat}, %	27	25
EUF_{cool}, %	0	0
EUF_{fuel}, %	17	19

5.5.2 SOEC operating pressure and CO_2 mass flow rate

The SOEC operating pressure affects system performance by shifting the reaction equilibrium and modifying the polarization curve, which alters the electrical energy requirement for the electrolysis process. The CO_2 mass flow rate influences the outlet gas composition and product distribution in the P2F module. Fig. 16 shows how the SOEC pressure and CO_2 mass flow rate affect key performance metrics (polarization curves, outlet temperature and gas composition) under a fixed inlet gas molar ratio of CO_2:H_2O:CO:H_2 = 1:4.4:0.05:0.05.



(a) (b)



(c)

Fig. 15. Effect of the SOEC operating pressure and CO_2 mass flow rate on: (a) polarization curves, (b) outlet temperature and (c) outlet gas composition.

In Fig. 16 (a), elevated operating pressure reduces current density under equivalent cell voltages, whereas the CO_2 mass flow rate has a negligible influence on polarization behavior. This operational characteristic reduces current density requirements at fixed voltage conditions, which improves the system energy utilization factor through reduced co-electrolysis electricity demand.

Fig. 16 (b) reveals that operating pressure and CO_2 mass flow rate exert negligible effects on the thermal-neutral voltage, which remains consistently at 1.32 V. When the operating voltage exceeds this threshold (>1.32 V), elevated pressure enhances gas-phase diffusion efficiency. As a result, concentration polarization is mitigated and overvoltage is reduced. As overvoltage decreases, Joule heating is reduced and the SOEC outlet temperature falls. Conversely, at sub-thermal-neutral voltages, increased pressure reduces the Nernst potential. This amplifies overvoltage and Joule heat generation, which elevates the outlet temperature.

Fig. 16 (c) shows that higher operating pressures elevate the CO_2 and H_2O concentrations in the outlet gas while reducing the CO and H_2 proportions, which indicates pressure-induced inhibition of co-electrolysis product formation. This inverse relationship suggests that elevated pressures may detrimentally affect the CO_2-H_2O co-electrolysis efficiency within SOEC systems. The CO_2 mass flow rate has only a limited influence on the composition of the cathode outlet gases. Increasing the CO_2 flow rate only marginally reduces the CO concentration in the exhaust stream while proportionally elevating the content of the other three gaseous components.

5.5.3 SOEC charging and discharging operating voltage

The SOEC operating voltage also affects both the electrical energy requirement of the SOEC and the outlet gas composition. It therefore influences system performance. Fig. 17 illustrates the effect of the SOEC charging and discharging voltages on the system energy and exergy utilization factors under the design conditions that the CO_2 mass flow rate during discharging is three times that during charging. As shown in Fig. 17 (a) and (b), the maximum system energy (81%) and exergy (58%) utilization factors are

achieved at 1.4 V for both charging and discharging. Increasing voltage elevates SOEC electricity demand while maintaining a constant CO_2 electrolysis mass flow rate. Methane production remains unchanged, but the energy utilization factor decreases. Within the 1.35-1.4 V range, a higher voltage increases the SOEC outlet gas temperature. This increases thermal exergy through higher-grade heat storage and improves the system exergy utilization factor. Beyond
1.4 V, excessive electricity consumption dominates and the exergy utilization factor decreases progressively.

Fig. 17 (c) reveals that the discharging power ratio is solely influenced by the discharging voltage. As the voltage increases from 1.35 V to 1.45 V, the discharging power ratio decreases by 16% but remains above 100%. This confirms the system's ability to continue exporting net electricity to the grid or directly supplying electricity to end-users during discharging.

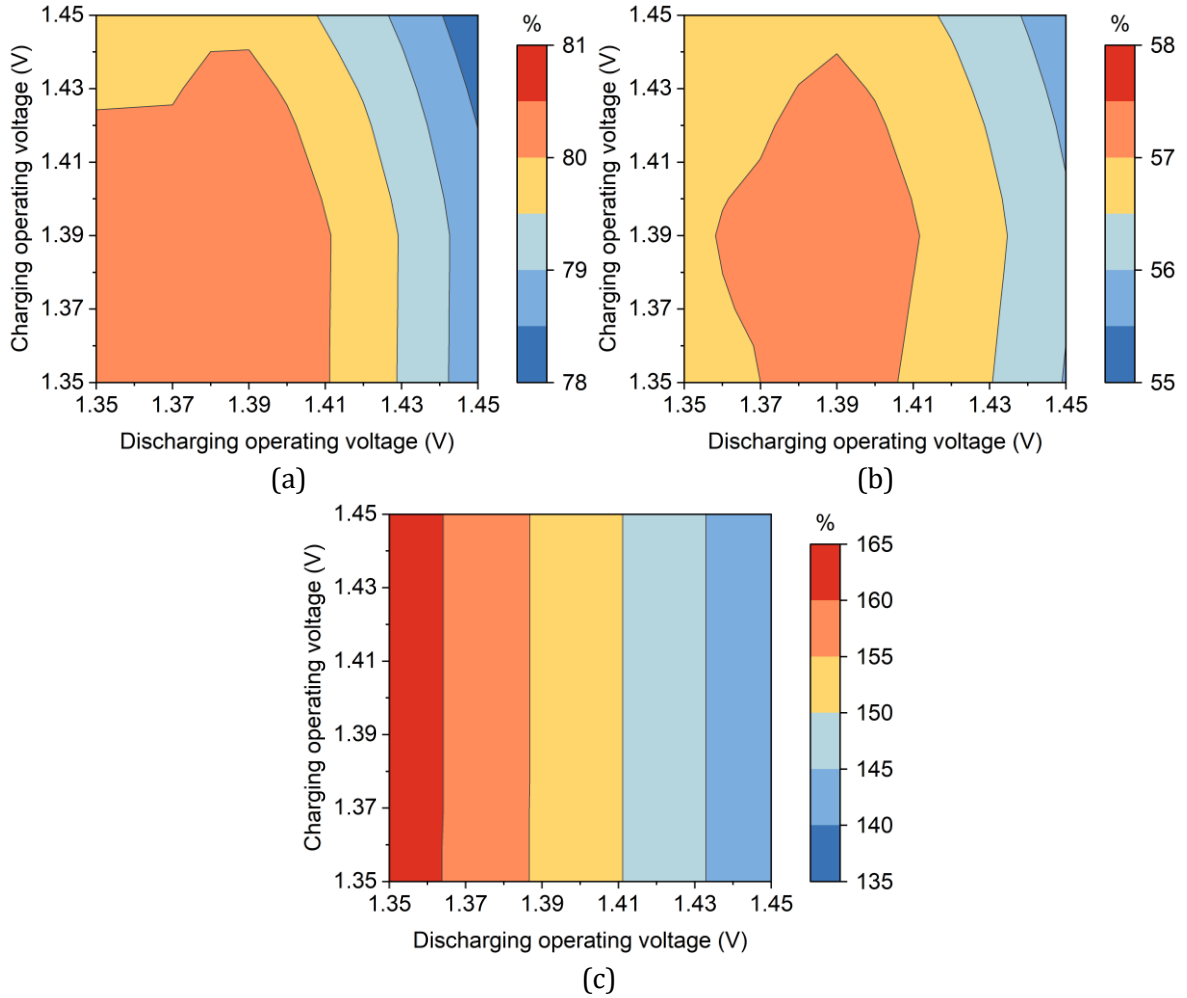


Fig. 16. Effect of the SOEC charging and discharging operating voltage on: (a) system energy utilization factor, *EUF*, (b) system exergy utilization factor, *ExUF* and (c) discharging power ratio, β.

5.6 Effect of external waste heat quantity and temperature

The H-TES enables the integrated use of both internal module heat and external waste heat. The stored thermal energy can then be used for CO_2 reheating at the expander inlets or for direct heating supply to

end-users. As such, the quantity (α) and temperature (T_{waste}) of external waste heat play a crucial role in influencing the system performance metrics. Fig. 18 illustrates the impact of α and T_{waste} on the individual energy utilization factors.

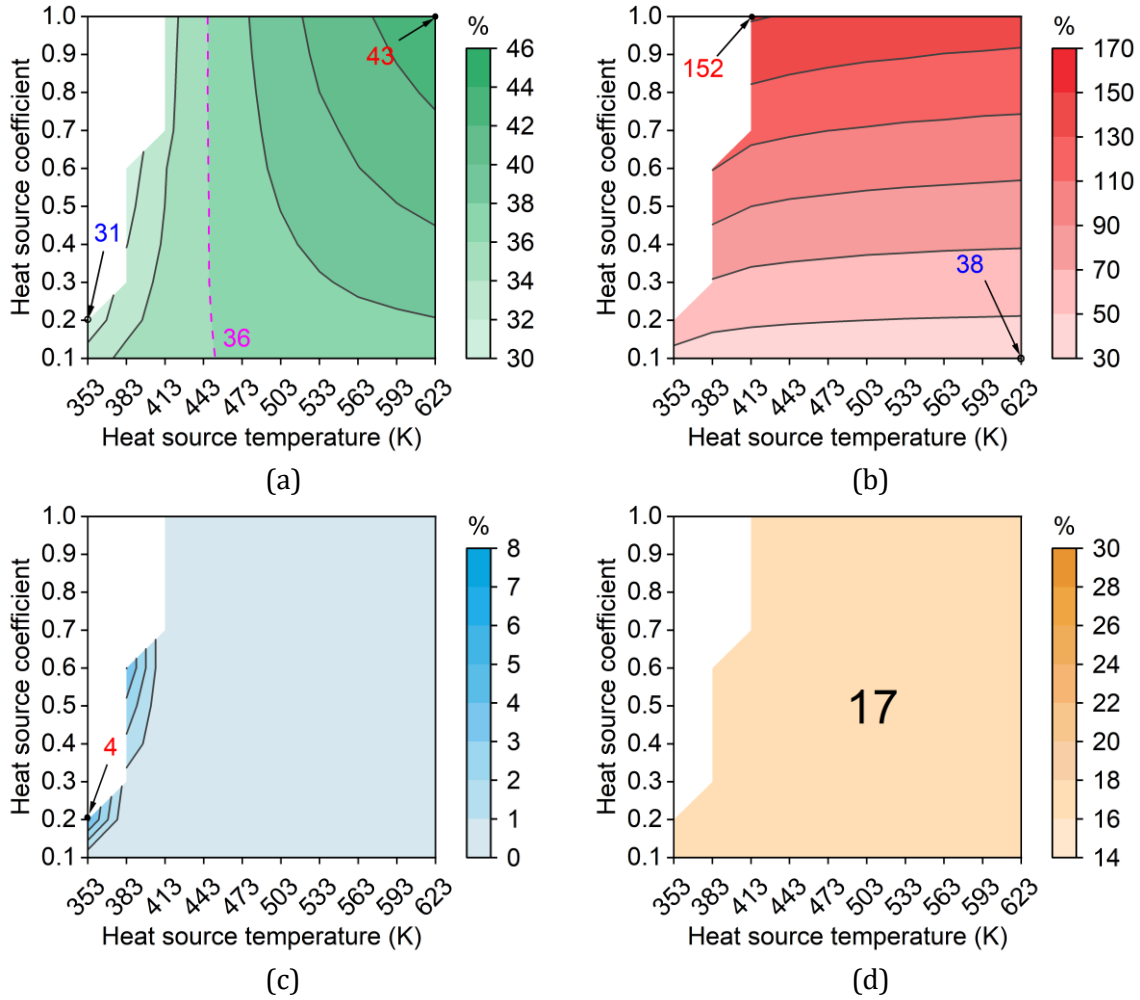


Fig. 17. Effect of the external waste heat quantity and temperature on: (a) electricity utilization factor, EUF_{ele}, (b) heating utilization factor, EUF_{heat}, (c) cooling utilization factor, EUF_{cool} and (d) fuel utilization factor, EUF_{fuel}.

In Fig. 18 (a), the electricity utilization factor varies between 31% and 43% depending on α and T_{waste}. When T_{waste} < 443 K, the CO_2 temperature at the expander inlets decreases, which reduces electricity output through constrained thermal expansion potential. Effective enhancement of the electricity utilization factor requires maintaining T_{waste} ≥ 443 K to ensure sufficient thermal energy for stable expansion processes.

In Fig. 18 (b), the heating utilization factor can increase by up to 152% as α increases and T_{waste} decreases. Higher T_{waste} raises the thermal grade of the H-TES and more heat is redirected to reheat CO_2 at the expander inlets, which improves the electricity utilization factor but reduces the heating utilization factor. Meanwhile, some external waste heat stored in the H-TES bypasses the reheating process and is delivered directly as external heating output. Therefore, the integration of external waste heat significantly enhances the heating utilization factor, especially under conditions of high heat quantity and low

temperature.

Fig. 18 (c) indicates that the cooling utilization factor achieves a maximum of 4% at T_{waste} = 353 K with α = 0.2, and it is activated when T_{waste} < 404 K, under which conditions cooling production escalates with increasing heat source coefficient. In contrast, Fig. 18 (d) confirms that the fuel utilization factor remains constant at 17% and is unaffected by variations in external waste heat parameters, which demonstrates the decoupling between fuel synthesis and thermal recovery processes.

Fig. 19 shows the effect of α and T_{waste} on the system energy and exergy utilization factors. Fig. 19 (a) demonstrates that the peak system energy utilization factor (202%) is achieved with increasing α and decreasing T_{waste}. Increased α amplifies usable heating output to end-users, while reduced T_{waste} lowers the H-TES thermal energy demand for CO_2 reheating at the expander inlets. This reduces heat-to-power conversion losses and enhances the system energy utilization factor. Fig. 19 (b) shows that the peak system exergy utilization factor (107%) is achieved with increasing α and T_{waste}. Higher α and T_{waste} significantly elevate the quality of waste heat. Consequently, the system exergy output increases.

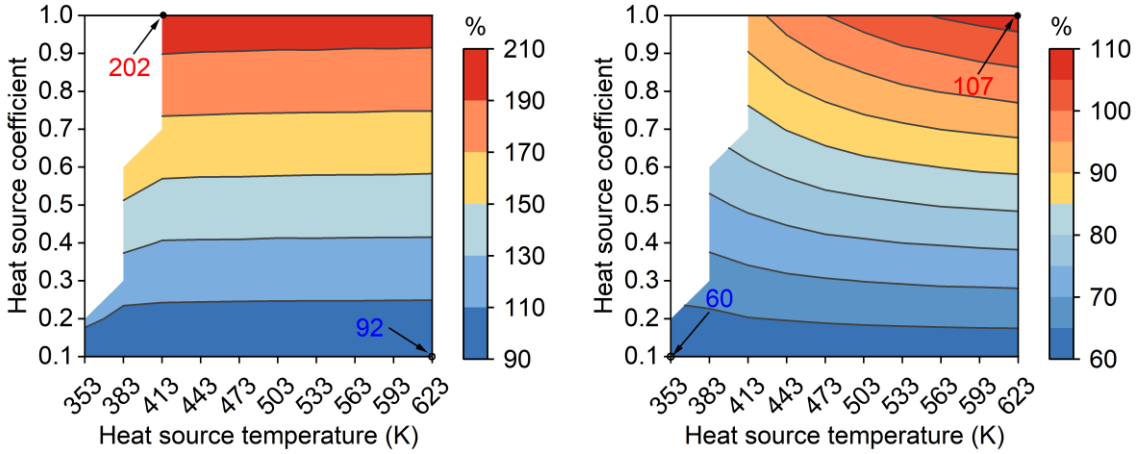


Fig. 18. Effect of the external waste heat quantity and temperature on: (a) system energy utilization factor, *EUF* and (b) system exergy utilization factor, *ExUF*.

5.7 Optimal results of system and individual performance metrics

The proposed CO_2-based polygeneration system was optimized through genetic-algorithm-driven single-objective analysis. Seven performance indices were evaluated, namely the energy, exergy, electricity, heating, cooling and fuel utilization factors (*EUF*, *ExUF*, EUF_{ele}, EUF_{heat}, EUF_{cool} and EUF_{fuel}), as well as the *LCOE*. Comparative studies were conducted under two configurations: with and without external waste heat integration. Core optimization parameters included compression and expansion stages (1-10), H-TES heat allocation ratio (50-100%), CO_2 secondary distribution coefficient (0-2), adsorption/desorption temperatures (298-310 K/353-393 K) and charging/discharging voltages (1.35-1.45 V). For waste heat scenarios, supplementary parameters included waste heat source coefficient (0-1) and waste heat temperature range (353-623 K).

Table 6 presents optimal performance metrics under no-waste-heat conditions and highlights the

consistent configurations for the peak system energy (146%), heating (79%) and cooling (19%) utilization factors. A higher number of compression stages reduces the H-TES storage temperatures. This decreases the CO_2 reheating demand before expansion and enables efficient cold energy storage at the outlets of the third to fifth expanders. Surplus heat is redirected to end-users, which boosts the energy utilization factor, with an H-TES heat allocation ratio of 65%. For the maximum electricity and fuel utilization factors, 95% of the heat stored in the H-TES is allocated to reheating at the expander inlets. This increases electricity generation and fuel output by enhancing CO_2 participation in co-electrolysis and fuel synthesis. To optimize exergy utilization, reducing exergy destruction during energy conversion processes is crucial. Lower compression stages generate higher-temperature compression heat, and adjusting the H-TES heat allocation ratio reduces exergy losses and improves the system exergy utilization. For the economic indicator *LCOE*, the minimum value is \$0.075/kWh, which corresponds to the same configuration as the one with the highest EUF_{ele}. This suggests that, when economic performance is driven primarily by the amount of electricity produced without considering cross-regional fuel sales, higher electricity output leads to better economic performance.

Table 6. Optimization results without external waste heat.

Optimization objectives	***EUF***	***ExUF***	EUF_{ele}	EUF_{heat}	EUF_{cool}	EUF_{fuel}	***LCOE***
Compression and expansion stage numbers	(10, 5)	(2, 2)	(2, 2)	(10, 5)	(10, 5)	(6, 5)	(2, 2)
H-TES heat allocation ratio, ζ, %	65	76	95	65	65	93	95
CO_2 secondary distribution coefficient, λ, -	0.00	2.00	0.00	0.00	0.00	1.15	0.00
Adsorption temperature, K	309	307	298	309	309	312	298
Desorption temperature, K	354	353	393	354	354	381	393
Charging operating voltage, V	1.40	1.39	1.35	1.40	1.40	1.39	1.35
Discharging operating voltage, V	1.40	1.39	1.35	1.40	1.40	1.39	1.35
Discharging power ratio, β, %	140	101	233	140	140	100	233
EUF, %	146	91	80	146	146	85	80
ExUF, %	57	60	56	57	57	53	56
EUF_{ele}, %	30	29	39	30	30	30	39
EUF_{heat}, %	79	37	28	79	79	31	28
EUF_{cool}, %	19	4	0	19	19	2	0
EUF_{fuel}, %	18	20	13	18	18	22	13

Optimization objectives	***EUF***	***ExUF***	EUF_{ele}	EUF_{heat}	EUF_{cool}	EUF_{fuel}	***LCOE***
LCOE, \$/kWh	0.092	0.098	0.075	0.092	0.092	0.21	0.075

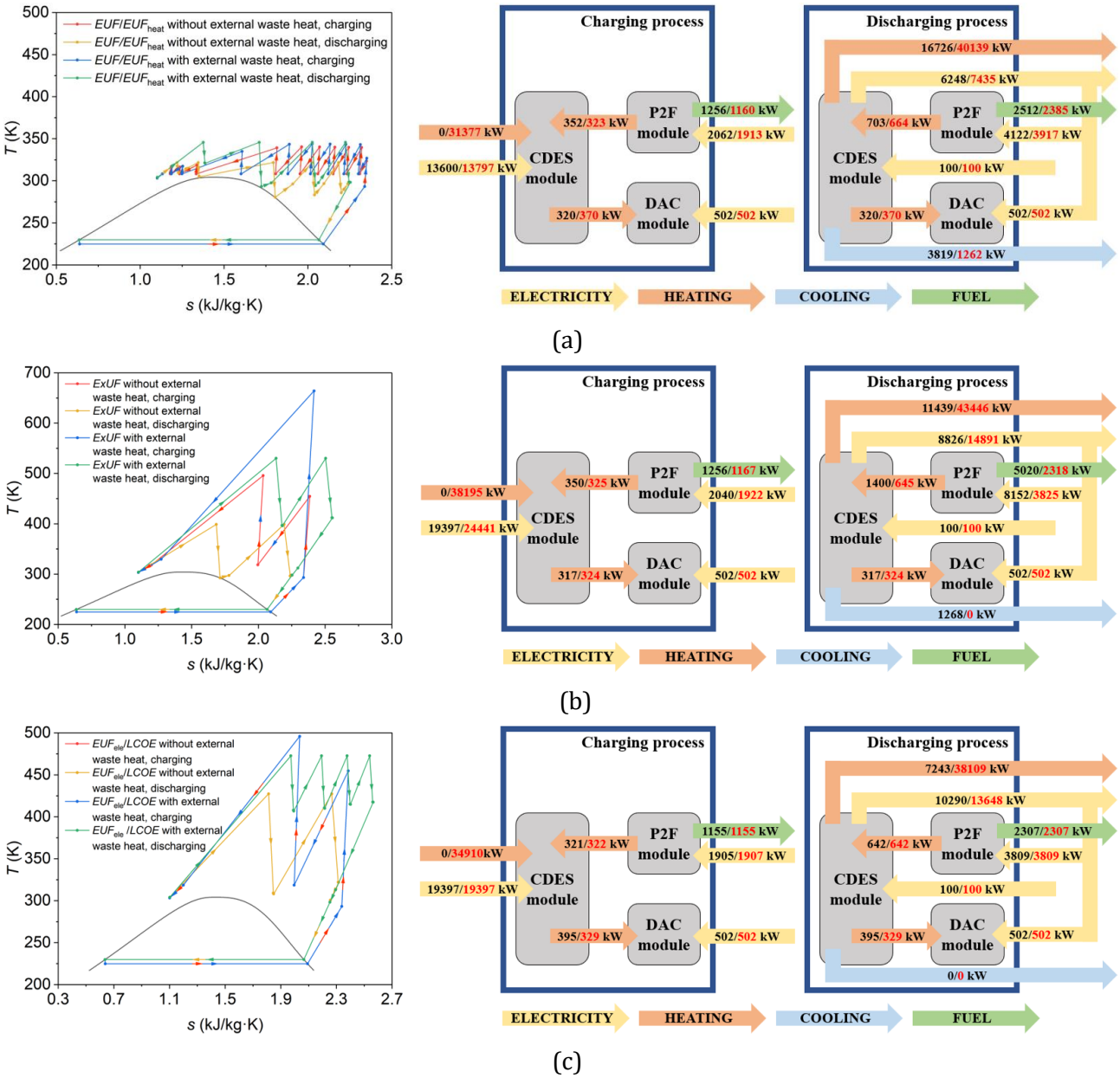
Table 7 demonstrates that external waste heat integration substantially enhances the overall and individual energy and exergy utilization factors, with the energy utilization factor increasing from 146% to 253%, the exergy utilization factor from 60% to 112%, the electricity utilization factor from 39% to 52% and the heating utilization factor from 79% to 193%. Elevated waste heat temperatures maximize CO_2 reheating at the expander inlets and boost electricity output, whereas lower temperatures prioritize direct heating supply. This improves the energy, exergy and heating utilization factors. The cooling utilization factor remains unaffected by waste heat inputs. High-temperature waste heat additionally supports the P2F module operation through surplus electricity generation. This elevates the fuel utilization factor via intensified co-electrolysis. With the introduction of waste heat, the minimum *LCOE* decreases from \$0.075/kWh to \$0.039/kWh. This demonstrates that incorporating waste heat can significantly enhance the system's economic performance and improve its competitiveness in terms of cost.

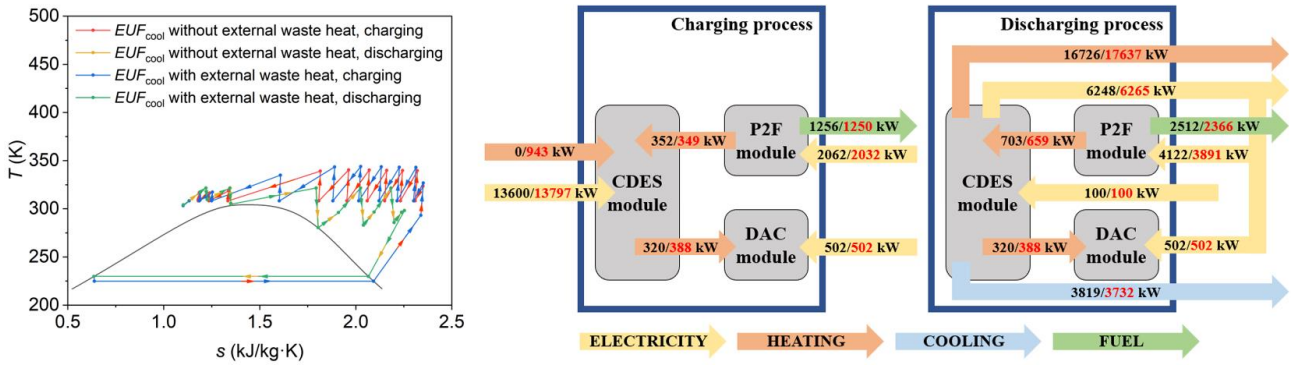
Table 7. Optimization results with external waste heat.

Optimization objectives	***EUF***	***ExUF***	EUF_{ele}	EUF_{heat}	EUF_{cool}	EUF_{fuel}	***LCOE***
Compression and expansion stage numbers	(9, 4)	(1, 2)	(2, 4)	(9, 4)	(9, 5)	(6, 6)	(2, 4)
H-TES heat allocation ratio, ζ, %	50	66	89	50	60	79	89
CO_2 secondary distribution coefficient, λ, -	0.01	0.01	0.01	0.01	0.01	2.00	0.01
Adsorption temperature, K	306	307	307	306	301	311	307
Desorption temperature, K	379	357	368	379	389	361	368
Charging operating voltage, V	1.35	1.36	1.36	1.35	1.39	1.39	1.36
Discharging operating voltage, V	1.36	1.35	1.35	1.36	1.36	1.39	1.35
Heat source coefficient, α, -	1.00	1.00	1.00	1.00	0.03	0.93	1.00
Waste heat temperature, K	454	622	622	454	475	609	622
Discharging power ratio, β, %	165	336	306	165	139	100	306
EUF, %	253	198	211	253	150	196	211
ExUF, %	80	112	108	80	57	79	108
EUF_{ele}, %	36	48	52	36	30	34	52
EUF_{heat}, %	193	139	146	193	85	137	146

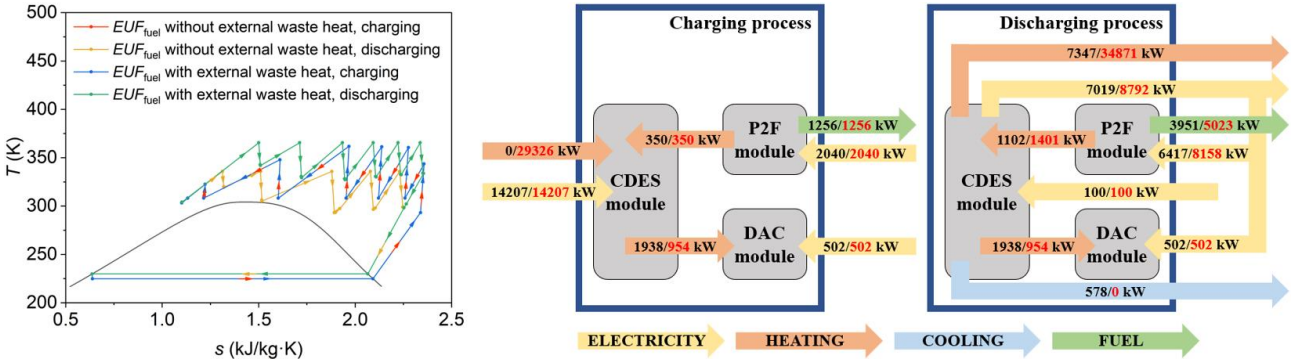
Optimization objectives	***EUF***	***ExUF***	***EUF*$_{ele}$**	***EUF*$_{heat}$**	***EUF*$_{cool}$**	***EUF*$_{fuel}$**	***LCOE***
EUF_{cool}, %	6	0	0	6	19	0	0
EUF_{fuel}, %	17	11	13	17	17	25	13
LCOE, \$/kWh	0.057	0.072	0.039	0.057	0.086	0.088	0.039

Fig. 20 presents the *T-s* diagrams and the corresponding energy flow diagrams for the seven optimization cases, both without and with external waste heat.





(d)



(e)

Fig. 19. *T-s* diagrams and energy flow diagrams for the following optimization cases: (a) optimal energy and heating utilization factors, (b) optimal exergy utilization factor, (c) optimal electricity utilization factor and levelized cost of energy, (d) optimal cooling utilization factor and (e) optimal fuel utilization factor. Black and red figures represent values without and with external waste heat, respectively. (For interpretation of the references to color in this figure legend, the reader is referred to the Web version of this article.)

Fig. 20 (a) shows the system optimized for the energy and heating utilization factors, where the number of compression stages is set to ten. This leads to lower compression heat temperatures, limiting effective energy conversion. Without external waste heat, the system produces 1520 kW of electricity and 16700 kW of heating. With external waste heat, the system generates 2920 kW of electricity and 40100 kW of heating. Fig. 20 (b) focuses on the optimal exergy utilization factor. Higher compression heat temperatures reduce energy conversion losses and improve the exergy utilization factor. The system generates cooling at the outlets of the first expansion stage without external waste heat.

The configuration for which the electricity utilization factor and the levelized cost of energy are both optimized is shown in Fig. 20 (c). With high-quality compression heat, 95% of the heat stored in the H-TES is used for CO_2 preheating and the electrical output reaches 5880 kW without external waste heat. When external waste heat is integrated, the H-TES heat allocation ratio drops to 89%, while the electrical output increases to 9240 kW. Fig. 20 (d) shows the system under the optimal cooling utilization factor. Due to low CO_2 temperatures at the inlets of the third to fifth expansion stages, cooling outputs are 3820 kW without external waste heat and 3730 kW with external waste heat, with no significant change from

external heat integration. Fig. 20 (e) illustrates the system under the optimal fuel utilization factor. When the discharging power ratio exceeds 100%, more CO_2 is directed to the P2F module. As a result, the total fuel output reaches 5210 kW without external waste heat and 6280 kW with external waste heat.

5.8 Comparative analysis of system performance metrics

This section provides a comprehensive comparison between the proposed CO_2-based polygeneration system and representative CDES-CHP, CDES-CCP and CDES-CCHP configurations reported in the literature, as summarized in Table 8. The analysis emphasizes both technical efficiency and economic viability, and reveals the added value of integrating fuel production and multi-energy cascading within a unified CO_2 conversion chain.

5.8.1 Technical performance comparison

The *EUF* serves as a primary metric for evaluating the system's capacity to convert input energy into useful outputs (electricity, heating, cooling and fuel). Without the use of external waste heat, it achieves an *EUF* of 146%, which exceeds most reported values for CHP and CCP systems (63%-112%) and significantly outperforms those of typical CCHP configurations (119%-158%). This improvement is primarily attributed to the inclusion of fuel production, which notably increases the total useful energy output.

When external waste heat (e.g., from industrial processes or renewable heat sources) is integrated into the system, the *EUF* increases to 253%, more than doubling the best values reported in existing studies. This reflects the system's ability to cascade heat across multiple temperature levels and energy applications, thereby enhancing overall energy utilization performance.

The *ExUF*, a more rigorous metric for evaluating the quality of energy conversion, further underscores the advantages of the proposed design. Existing systems typically achieve *ExUF* values in the range of 31%-58% and only a few exceed 50%. The proposed system achieves an *ExUF* of 60% without waste heat and 112% with waste heat integration. This highlights the effective preservation and deployment of exergy across the full spectrum of energy carriers.

This is particularly significant because exergy losses are often concentrated in low-value thermal outputs. By leveraging CO_2 as both a working fluid and a storage medium and integrating thermal management strategies, the proposed system reduces these losses and achieves a more balanced and efficient exergy profile.

5.8.2 Economic performance comparison

Beyond technical performance, economic competitiveness is essential for real-world adoption. The *LCOE*, a widely accepted metric for comparing life-cycle energy costs, is significantly lower for the proposed system: \$0.075/kWh without external waste heat and \$0.039/kWh with waste heat integration. In comparison, the reference systems report *LCOE*s ranging from \$0.068/kWh to \$0.17/kWh, with most falling above \$0.10/kWh. The cost advantage of the proposed design arises from the efficient cascading use of thermal energy, the added
value of co-produced fuels and the balanced output of heating and cooling services. Moreover, the system's design, particularly its 10 MW scale and 6-h charge and discharge cycle, aligns well with large-scale

implementations reported in the literature and reinforces its feasibility and scalability for real-world deployment.

Table 8. Comparative performance of the proposed CO_2-based polygeneration system with CDES-CHP, CDES-CCP and CDES-CCHP systems.

Reference	**Type**	***EUF*, %**	***ExUF*, %**	***LCOE*, $·kWh^{-1}**	**Scale, MW**	**Charge/Discharge period, h**
Hao et al. [51]	CDES-CHP	88	--	--	10	Charge: 7.5/Discharge: 5
Xu et al. [52]	CDES-CHP	63	31	0.087	1	Charge: 2/Discharge: 9.8
Sun et al. [53]	CDES-CCP	79	58	0.15	7	Charge/Discharge: 8
Wang et al. [54]	CDES-CCP	112	--	0.10	10	Charge/Discharge: 8
Liu et al. [55]	CDES-CCHP	134	--	--	2	--
Zhang et al. [56]	CDES-CCHP	119	--	--	0.7	--
Deng et al. [57]	CDES-CCHP	158	51	0.10-0.17	25	Charge/Discharge: 6
Xu et al. [58]	CDES-CCHP	--	56	--	5	Charge/discharge: 6
Xu et al. [59]	CDES-CCHP	--	49	0.068	10	Charge/Discharge: 4
Proposed system without external waste heat	--	146	60	0.075	10	Charge/Discharge: 6
Proposed system with external waste heat	--	253	112	0.039	10	Charge/Discharge: 6

6. Conclusions

This study presents a CO_2-based polygeneration system that integrates electricity, heating, cooling and fuel production to meet diverse energy demands. The system stores energy during charging and dispatches energy according to demand during discharging. Through thermodynamic modeling, its performance is evaluated using seven key indicators: the energy, exergy, electricity, heating, cooling and fuel utilization factors, together with the levelized cost of energy. These multidimensional metrics provide a comprehensive assessment of operational effectiveness and establish a framework for optimizing

system performance under different energy supply conditions.

The system exhibits strong adaptability, with negligible performance variations when the CO_2 mass flow rate at the DAC outlet is altered. This indicates good scalability across different application scenarios. Notably, integrating CO_2 capture, storage and utilization leads to a 7.9% improvement in the overall energy utilization factor when the CO_2 mass flow ratio between CDES and DAC increases from 200 to 600. In addition, the stage-number optimization shows that a (10, 5) compression and expansion stage configuration is favorable for multioutput energy conversion under the fixed-parameter condition considered in this study.

The process-control parameters exhibit distinct output-modulation characteristics. The CO_2 secondary distribution coefficient governs the balance between power generation and fuel production, whereas the H-TES heat allocation ratio determines the coordination between power and heating output. Under specific expansion-stage configurations (1 or 3-6) and low heat allocation ratios, thermodynamic analysis reveals a staged energy-recovery pattern in which cooling generation becomes localized at the downstream expander outlets. This demonstrates the spatiotemporal energy-harvesting characteristics of multi-stage expansion.

External waste heat affects system performance in different ways. Higher source temperatures enhance the electricity utilization factor while reducing the heating utilization factor. Threshold analysis indicates that the electricity utilization factor improves only when the waste heat temperature exceeds 443 K, identifying this value as the critical temperature for optimizing dual-energy output performance.

The system is modular and can be reconfigured from CO_2-H_2O co-electrolysis to standalone H_2O electrolysis for hydrogen generation. This offers flexibility in allocating surplus electrical capacity either to hydrogen production or to direct electricity supply. The optimal operating voltage is 1.4 V, and the peak utilization factor is obtained under controlled SOEC inlet conditions (CO_2:H_2O:CO:H_2 molar ratio = 1:4.4:0.05:0.05), which demonstrates voltage-dependent performance optimization through gas-composition regulation.

The optimization results indicate that, without waste heat integration, the system achieves optimal *EUF*, *ExUF* and *LCOE* values of 146%, 60% and \$0.075/kWh, respectively. With waste heat integration, these metrics improve significantly to 253%, 112% and \$0.039/kWh, respectively. This confirms a marked performance advantage over existing CDES-CHP, CDES-CCP and CDES-CCHP systems.

Overall, the proposed system offers a versatile energy architecture capable of delivering multiple energy vectors tailored to sector-specific demands. It is well-suited for sustainable urban environments, off-grid energy hubs and multi-nodal energy networks (e.g., offshore ports and energy islands), and is well aligned with the principles of circular energy economies.

Acknowledgements

This work was supported by the National Natural Science Foundation of China (Grant Nos. 52394205 and 51906150), the National Science and Technology Major Project (Grant No. 2026ZD1702401), the Future

Foundation of Energy Science (Grant No. WLNY-MS-2022-010) and the Open Fund Project of State Key Laboratory of Clean Energy Utilization (Grant No. ZJUCEU2022022). The work was also supported by the UK Engineering and Physical Sciences Research Council (EPSRC) [grant numbers EP/Y017471/1 and EP/S032622/1]. Data supporting this publication can be obtained on request from thameswalker@outlook.com and cep-lab@imperial.ac.uk. For the purpose of Open Access, the authors have applied a CC BY public copyright license to any Author Accepted Manuscript version arising from this submission.

References

[1] Solangi YA, Magazzino C. Evaluating financial implications of renewable energy for climate action and sustainable development goals. Renewable and Sustainable Energy Reviews. 2025;212:115390.

[2] Zhao Y, Zhao CY, Markides CN, Wang H, Li W. Medium- and high-temperature latent and thermochemical heat storage using metals and metallic compounds as heat storage media: A technical review. Applied Energy. 2020;280:115950.

[3] Forootan MM, Ahmadi A. Machine learning-based optimization and 4E analysis of renewable-based polygeneration system by integration of GT-SRC-ORC-SOFC-PEME-MED-RO using multi-objective grey wolf optimization algorithm and neural networks. Renewable and Sustainable Energy Reviews. 2024;200:114616.

[4] Liu Z-F, Luo X-F, Hou X-X, Yu J-L, Li J-X. Generalized energy pool-driven regional integrated energy system dispatch considering multi-time scale synergy carbon-storage game. Renewable and Sustainable Energy Reviews. 2025;217:115752.

[5] Lüth A, Keles D. Risks, strategies, and benefits of offshore energy hubs: A literature-based survey. Renewable and Sustainable Energy Reviews. 2024;203:114761.

[6] Zhao Y, Li M, Wang K, Sciacovelli A, Qin C, Lecompte S, et al. Thermo-mechanical energy storage technologies: Innovations, challenges and future directions. Frontiers in Energy. 2025;19:115-6.

[7] Chen L, Zhang L, Guo W, Lian H, Wang Y, Ye K, et al. Dynamic analysis of an adiabatic compressed air energy storage system with temperature-regulated in air tanks. Renewable and Sustainable Energy Reviews. 2024;206:114862.

[8] She X, Wang H, Zhang T, Li Y, Zhao X, Ding Y, et al. Liquid air energy storage – A critical review. Renewable and Sustainable Energy Reviews. 2025;208:114986.

[9] Zhao Y, Huang J, Song J, Ding Y. Thermodynamic investigation of a Carnot battery based multi-energy system with cascaded latent thermal (heat and cold) energy stores. Energy. 2024;296:131148.

[10] Wan Y, Wu C, Liu Y, Liu C, Li H, Wang J. A technical feasibility study of a liquid carbon dioxide energy storage system: Integrated component design and off-design performance analysis. Applied Energy. 2023;350:121797.

[11] Olympios AV, McTigue JD, Farres-Antunez P, Tafone A, Romagnoli A, Li YL, et al. Progress and prospects of thermo-mechanical energy storage-a critical review. Progress in Energy. 2021;3:022001.

[12] Huang J, Zhao Y, Song J, Huang S, Wang K, Rao Z, et al. A review of progress in thermo-mechanical energy storage technologies for combined cooling, heating and power applications. Frontiers in Energy. 2025;19:117-43.

[13] Bose S, Sengupta D, Rayder TM, Wang X, Kirlikovali KO, Sekizkardes AK, et al. Challenges and opportunities: Metal–organic frameworks for direct air capture. Advanced Functional Materials. 2023;34:2307478.

[14] Li H, Ren Z, Trivedi A, Srinivasan D, Liu P. Optimal planning of dual-zero microgrid on an island toward net-zero carbon emission. IEEE Transactions on Smart Grid. 2024;15:1243-57.

[15] Sami S, Gholizadeh M, Deymi-Dashtebayaz M. A comprehensive 5E analysis of synthetic natural gas production

through direct air capture and renewable hydrogen: Based on a specified-scale residential application. Renewable and Sustainable Energy Reviews. 2025;212:115376.
[16] Long-Innes R, Struchtrup H. Thermodynamic loss analysis of a liquid-sorbent direct air carbon capture plant. Cell Reports Physical Science. 2022;3:100791.
[17] Shi X, Xiao H, Azarabadi H, Song J, Wu X, Chen X, et al. Sorbents for the direct capture of CO_2 from ambient air. Angew Chem Int Ed Engl. 2020;59:6984-7006.
[18] Zheng J, Chen X, Ma J, Liang C. Characterization of the carbonation reaction of potassium-based composite adsorbents for direct air capture of CO_2. Separation and Purification Technology. 2025;363:132099.
[19] Liu W, Lin YC, Jiang L, Ji Y, Yong JY, Zhang XJ. Thermodynamic exploration of two-stage vacuum-pressure swing adsorption for carbon dioxide capture. Energy. 2022;241:122901.
[20] Balasubramaniam BM, Thierry P-T, Lethier S, Pugnet V, Llewellyn P, Rajendran A. Process-performance of solid sorbents for Direct Air Capture (DAC) of CO_2 in optimized temperature-vacuum swing adsorption (TVSA) cycles. Chemical Engineering Journal. 2024;485:149568.
[21] Jin Y, Lin H, Liu Y, An H, Lee JS. Optimizing amine-based adsorbents for direct air capture: A comprehensive review of performance under diverse climatic conditions. Renewable and Sustainable Energy Reviews. 2025;217:115782.
[22] Hua Y, Ahmadi Y, Kim K-H, Yu W. Functional strategies and performance assessment of covalent organic framework–based materials for carbon dioxide capture. Renewable and Sustainable Energy Reviews. 2025;222:115949.
[23] Haertel CJJ, McNutt M, Ozkan M, Aradóttir ESP, Valsaraj KT, Sanberg PR, et al. The promise of scalable direct air capture. Chem. 2021;7:2831-4.
[24] Yafiee OA, Mumtaz F, Kumari P, Karanikolos GN, Decarlis A, Dumée LF. Direct air capture (DAC) vs. Direct ocean capture (DOC)–A perspective on scale-up demonstrations and environmental relevance to sustain decarbonization. Chemical Engineering Journal. 2024;497:154421.
[25] McQueen N, Gomes KV, McCormick C, Blumanthal K, Pisciotta M, Wilcox J. A review of direct air capture (DAC): scaling up commercial technologies and innovating for the future. Progress in Energy. 2021;3:032001.
[26] Sabatino F, Grimm A, Gallucci F, van Sint Annaland M, Kramer GJ, Gazzani M. A comparative energy and costs assessment and optimization for direct air capture technologies. Joule. 2021;5:2047-76.
[27] Fahr S, Powell J, Favero A, Giarrusso AJ, Lively RP, Realff MJ. Assessing the physical potential capacity of direct air capture with integrated supply of low-carbon energy sources. Greenhouse Gases: Science and Technology. 2021;12:170-88.
[28] Mohan A, Cheng F, Luo H, Greig C, Larson E, Jenkins JD. Direct air capture integration with low-carbon heat: Process engineering and power system analysis. Energ Convers Manage. 2024;322:119136.
[29] Bertoni L, Roussanaly S, Riboldi L, Anantharaman R, Gazzani M. Integrating direct air capture with small modular nuclear reactors: understanding performance, cost, and potential. Journal of Physics: Energy. 2024;6:025004.
[30] Ge B, Zhang M, Hu B, Wu D, Zhu X, Eicker U, et al. Innovative process integrating high temperature heat pump and direct air capture. Applied Energy. 2024;355:122229.
[31] Zhu X, Ge T, Yang F, Wang R. Design of steam-assisted temperature vacuum-swing adsorption processes for efficient CO_2 capture from ambient air. Renewable and Sustainable Energy Reviews. 2021;137:110651.
[32] McQueen N, Psarras P, Pilorge H, Liguori S, He J, Yuan M, et al. Cost analysis of direct air capture and sequestration coupled to low-carbon thermal energy in the United States. Environ Sci Technol. 2020;54:7542-51.
[33] Qi M, Vo DN, Yu H, Shu C-M, Cui C, Liu Y, et al. Strategies for flexible operation of power-to-X processes coupled with renewables. Renewable and Sustainable Energy Reviews. 2023;179:113282.

[34] Qi M, Lee J, Hong S, Kim J, Liu Y, Park J, et al. Flexible and efficient renewable-power-to-methane concept enabled by liquid CO_2 energy storage: Optimization with power allocation and storage sizing. Energy. 2022;256:124583.
[35] Hao Y, He Q, Du D. A trans-critical carbon dioxide energy storage system with heat pump to recover stored heat of compression. Renew Energ. 2020;152:1099-108.
[36] Zheng P, Hao J, Zhang Z, Yang J, Li X, Yue Y. Analysis of heat transfer characteristics of a novel liquid CO_2 energy storage system based on two-stage cold and heat storage. Frontiers in Energy. 2024;19:193-204.
[37] Liu A, Zhao P, Sun J, Xu W, Ma N, Wang J. A new energy management strategy of a hybrid energy storage system with compressed carbon dioxide energy storage and power-to-gas device based on the system volume optimization. Appl Therm Eng. 2025;269:126161.
[38] Hao J, Zheng P, Song Y, Zhang Z, Yang J, Yue Y. A carbon dioxide energy storage system with high-temperature graded heat storage structure: Thermodynamic intrinsic cycle construction and performance analysis. Frontiers in Energy. 2025;19:240-55.
[39] Liu Z, Yan X, Wang S, Wei X, Zhang Y, Ding J, et al. Performance of compressed CO_2 energy storage systems with different liquefaction and storage scenarios. Fuel. 2024;359:130527.
[40] Sun W, Liu X, Yang X, Yang X, Liu Z. Design and thermodynamic performance analysis of a new liquid carbon dioxide energy storage system with low pressure stores. Energ Convers Manage. 2021;239:114227.
[41] Huang Q, Feng B, Liu S, Ma C, Li H, Sun Q. Dynamic operating characteristics of a compressed CO_2 energy storage system. Applied Energy. 2023;341:120985.
[42] Hao Y, Xu X, Wang F, Wang Y, Du J, Wu C, et al. Dynamic characteristics of gas-liquid type compressed CO_2 energy storage system with focus on high-pressure liquid energy release process. Energy. 2025;316:134502.
[43] Zhang Y, Wu Y, Yang K. Dynamic characteristics of a two-stage compression and two-stage expansion Compressed Carbon dioxide energy storage system under sliding pressure operation. Energ Convers Manage. 2022;254:115218.
[44] Zhao P, Xu W, Zhang S, Gou F, Wang J, Dai Y. Components design and performance analysis of a novel compressed carbon dioxide energy storage system: A pathway towards realizability. Energ Convers Manage. 2021;229:113679.
[45] Chae YJ, Lee JI. Thermodynamic analysis of compressed and liquid carbon dioxide energy storage system integrated with steam cycle for flexible operation of thermal power plant. Energ Convers Manage. 2022;256:115374.
[46] Tang B, Sun L, Xie Y. Comprehensive performance evaluation and optimization of a liquid carbon dioxide energy storage system with heat source. Appl Therm Eng. 2022;215:118957.
[47] Xu W, Zhao P, Liu A, Wu W, Wang J. Design and off-design performance analysis of a liquid carbon dioxide energy storage system integrated with low-grade heat source. Appl Therm Eng. 2023;228:120570.
[48] Fu H, He Q, Song J, Hao Y. Thermodynamic of a novel solar heat storage compressed carbon dioxide energy storage system. Energ Convers Manage. 2021;247:114757.
[49] Chen K-Q, Pu W-H, Zhang Q, Xing X-L, Xiong C, Guo M-D. Thermodynamic and economic assessment on the supercritical compressed carbon dioxide energy storage system coupled with solar thermal storage. J Energy Storage. 2021;41:102959.
[50] Tang J, Li Q, Werle S, Wang S, Yu H. Development and comprehensive thermo-economic analysis of a novel compressed CO_2 energy storage system integrated with high-temperature thermal energy storage. Energy. 2024;303:131941.
[51] Hao J, Zheng P, Li Y, Zhang Z, Zhang J, Yang J, et al. Study on the operational feasibility domain of combined heat and power generation system based on compressed carbon dioxide energy storage. Energy. 2024;291:130122.
[52] Xu W, Zhao P, Gou F, Wu W, Liu A, Wang J. A combined heating and power system based on compressed carbon dioxide energy storage with carbon capture: Exploring the technical potential. Energ Convers Manage. 2022;260:115610.

[53] Sun L, Tang B, Xie Y. Performance assessment of two compressed and liquid carbon dioxide energy storage systems: Thermodynamic, exergoeconomic analysis and multi-objective optimization. Energy. 2022;256:124648.
[54] Wang D, Wu J, Liu S, Shi D, Xie Y. Performance evaluation and optimization of a novel compressed CO_2 energy storage system based on gas-liquid phase change and cold-electricity cogeneration. Frontiers in Energy. 2025;19:205-26.
[55] Liu Z, Cao F, Guo J, Liu J, Zhai H, Duan Z. Performance analysis of a novel combined cooling, heating and power system based on carbon dioxide energy storage. Energ Convers Manage. 2019;188:151-61.
[56] Zhang Y, Lin Y, Lin F, Yang K. Thermodynamic analysis of a novel combined cooling, heating, and power system consisting of wind energy and transcritical compressed CO_2 energy storage. Energ Convers Manage. 2022;260:115609.
[57] Deng Y, Wang J, Cao Y, Zhang X, Zhang N, He G, et al. Technical and economic evaluation of a novel liquid CO_2 energy storage-based combined cooling, heating, and power system characterized by direct refrigeration with phase change. Appl Therm Eng. 2023;230:120833.
[58] Xu W, Zhao P, Ma N, Liu A, Wang J. Design and performance analysis of a combined cooling, heating and power system: Integration of an isobaric compressed CO_2 energy storage and heat pump cycle. J Energy Storage. 2024;91:112146.
[59] Xu W, Zhao P, Gou F, Liu A, Wu W, Wang J. Thermo-economic analysis of a combined cooling, heating and power system based on self-evaporating liquid carbon dioxide energy storage. Applied Energy. 2022;326:120032.
[60] Hidalgo D, Martín-Marroquín JM. Power-to-methane, coupling CO_2 capture with fuel production: An overview. Renewable and Sustainable Energy Reviews. 2020;132:110057.
[61] Huang C, Lin Z, Xu C, Zhang B, Ou S, Xue X, et al. The complementary role of E-fuel in decarbonizing transportation and stabilizing the power grid. Renewable and Sustainable Energy Reviews. 2025;224:116033.
[62] Cho HH, Strezov V, Evans TJ. Life cycle assessment of power-to-methane and renewable methane production technologies. Renewable and Sustainable Energy Reviews. 2024;206:114856.
[63] Arinelli LdO, Brigagão GV, Wiesberg IL, Teixeira AM, de Medeiros JL, Araújo OdQF. Carbon-dioxide-to-methanol intensification with supersonic separators: Extra-carbonated natural gas purification via carbon capture and utilization. Renewable and Sustainable Energy Reviews. 2022;161:112424.
[64] Kontou V, Grimekis D, Braimakis K, Karellas S. Techno-economic assessment of dimethyl carbonate production based on carbon capture and utilization and power-to-fuel technology. Renewable and Sustainable Energy Reviews. 2022;157:112006.
[65] Chireshe F, Petersen AM, Ravinath A, Mnyakeni L, Ellis G, Viljoen H, et al. Cost-effective sustainable aviation fuel: Insights from a techno-economic and logistics analysis. Renewable and Sustainable Energy Reviews. 2025;210:115157.
[66] Mbatha S, Cui X, Panah PG, Thomas S, Parkhomenko K, Roger A-C, et al. Comparative evaluation of the power-to-methanol process configurations and assessment of process flexibility. Energy Advances. 2024;3:2245-70.
[67] He T, Pachfule P, Wu H, Xu Q, Chen P. Hydrogen carriers. Nature Reviews Materials. 2016;1:16059.
[68] Andika R, Nandiyanto ABD, Putra ZA, Bilad MR, Kim Y, Yun CM, et al. Co-electrolysis for power-to-methanol applications. Renewable and Sustainable Energy Reviews. 2018;95:227-41.
[69] Ebbesen SD, Jensen SH, Hauch A, Mogensen MB. High temperature electrolysis in alkaline cells, solid proton conducting cells, and solid oxide cells. Chem Rev. 2014;114:10697-734.
[70] Min G, Park YJ, Hong J. Thermodynamic analysis of a solid oxide co-electrolysis cell system for its optimal thermal integration with external heat supply. Energ Convers Manage. 2020;225:113381.
[71] Zhang W, Zheng Y, Yu B, Wang J, Chen J. Electrochemical characterization and mechanism analysis of high temperature co-electrolysis of CO_2 and H_2O in a solid oxide electrolysis cell. International Journal of Hydrogen

Energy. 2017;42:29911-20.
[72] Kazempoor P, Braun RJ. Model validation and performance analysis of regenerative solid oxide cells for energy storage applications: Reversible operation. International Journal of Hydrogen Energy. 2014;39:5955-71.
[73] Calise F, Cappiello FL, Cimmino L, Cutolo L, Vicidomini M. Thermoeconomic comparison of alkaline, solid oxide and anion exchange membrane electrolyzers for power-to-gas applications. Renewable and Sustainable Energy Reviews. 2025;224:116115.
[74] Kamkeng ADN, Wang M. Long-term performance prediction of solid oxide electrolysis cell (SOEC) for CO_2/H_2O co-electrolysis considering structural degradation through modelling and simulation. Chemical Engineering Journal. 2022;429:132158.
[75] Fei Y, Li A, Zhang C, Tu H, Zhu L, Huang Z. Performance optimization of solid oxide electrolysis cell for syngas production by high temperature co-electrolysis via differential evolution algorithm with practical constraints. Energ Convers Manage. 2024;300:117911.
[76] Luo Y, Wu X-y, Shi Y, Ghoniem AF, Cai N. Exergy analysis of an integrated solid oxide electrolysis cell-methanation reactor for renewable energy storage. Applied Energy. 2018;215:371-83.
[77] Wang L, Rao M, Diethelm S, Lin T-E, Zhang H, Hagen A, et al. Power-to-methane via co-electrolysis of H_2O and CO_2: The effects of pressurized operation and internal methanation. Applied Energy. 2019;250:1432-45.
[78] Min G, Park YJ, Choi S, Hong J. Sensitivity analysis of a solid oxide co-electrolysis cell system with respect to its key operating parameters and optimization with its performance map. Energ Convers Manage. 2021;249:114848.
[79] Bian L, Duan C, Wang L, Chen Z, Hou Y, Peng J, et al. An all-oxide electrolysis cells for syngas production with tunable H_2/CO yield via co-electrolysis of H_2O and CO_2. Journal of Power Sources. 2021;482:228887.
[80] Kim S-W, Bae Y, Yoon KJ, Lee J-H, Lee J-H, Hong J. High-temperature electrolysis of CO_2–enriched mixtures by using fuel-electrode supported $La_{0.6}Sr_{0.4}CoO_3$/YSZ/Ni-YSZ solid oxide cells. Journal of Power Sources. 2018;378:369-74.
[81] Li Y, Li P, Hu B, Xia C. A nanostructured ceramic fuel electrode for efficient CO_2/H_2O electrolysis without safe gas. Journal of Materials Chemistry A. 2016;4:9236-43.
[82] Luo Y, Wu X-Y, Shi Y, Ghoniem AF, Cai N. Exergy efficiency analysis of a power-to-methane system coupling water electrolysis and sabatier reaction. ECS Transactions. 2017;78:2965-73.
[83] Drechsler C, Agar DW. Investigation of water co-adsorption on the energy balance of solid sorbent based direct air capture processes. Energy. 2020;192:116587.
[84] Drechsler C, Agar DW. Intensified integrated direct air capture - power-to-gas process based on H_2O and CO_2 from ambient air. Applied Energy. 2020;273:115076.
[85] Paulsen MM, Petersen SB, Lozano EM, Pedersen TH. Techno-economic study of integrated high-temperature direct air capture with hydrogen-based calcination and Fischer–Tropsch synthesis for jet fuel production. Applied Energy. 2024;369:123524.
[86] Emadi M, Barahimi V, Croiset E. Integrated direct air CO_2 capture and solid oxide electrolyzer for sustainable chemical production: Case studies of methanol and synthesis fuel. Journal of CO_2 Utilization. 2025;96:103096.
[87] Furst O, Wehrle L, Schmider D, Dailly J, Deutschmann O. Modeling, optimization and comparative assessment of power-to-methane and carbon capture technologies for renewable fuel production. Applied Energy. 2024;375:123972.
[88] Zhang M, Ge B, Gan Z, Liu S, Li S, Shi Y, et al. Integrated power to methanol processes with steam-assisted direct air capture. Energ Convers Manage. 2025;326:119505.
[89] Song J, Fan Y, Wang F, Shi X, Li C, Du J, et al. Thermodynamic analysis of a novel compressed carbon dioxide energy storage coupled dry methane reforming system with integrated carbon capture. Applied Energy. 2025;377:124769.

[90] Qi M, Park J, Landon RS, Kim J, Liu Y, Moon I. Continuous and flexible renewable-power-to-methane via liquid CO_2 energy storage: Revisiting the techno-economic potential. Renewable and Sustainable Energy Reviews. 2022;153:111732.
[91] Erans M, Sanz-Pérez ES, Hanak DP, Clulow Z, Reiner DM, Mutch GA. Direct air capture: process technology, techno-economic and socio-political challenges. Energ Environ Sci. 2022;15:1360-405.
[92] Dewevre F, Lacroix C, Loubar K, Poncet S. Carbon dioxide energy storage systems: Current researches and perspectives. Renew Energ. 2024;224:120030.
[93] Kar S, Kim D, Bin Mohamad Annuar A, Sarma BB, Stanton M, Lam E, et al. Direct air capture of CO_2 for solar fuel production in flow. Nat Energy. 2025;10:448-59.
[94] Vučković GD, Stojiljković MM, Vukić MV, Stefanović GM, Dedeić EM. Advanced exergy analysis and exergoeconomic performance evaluation of thermal processes in an existing industrial plant. Energ Convers Manage. 2014;85:655-62.
[95] Zhao Y, Liu M, Song J, Wang C, Yan J, Markides CN. Advanced exergy analysis of a Joule-Brayton pumped thermal electricity storage system with liquid-phase storage. Energ Convers Manage. 2021;231:113867.
[96] Du Y, Qin Y, Zhang G, Yin Y, Jiao K, Du Q. Modelling of effect of pressure on co-electrolysis of water and carbon dioxide in solid oxide electrolysis cell. International Journal of Hydrogen Energy. 2019;44:3456-69.
[97] Giglio E, Pirone R, Bensaid S. Dynamic modelling of methanation reactors during start-up and regulation in intermittent power-to-gas applications. Renew Energ. 2021;170:1040-51.
[98] Sayama S, Yamamoto S. A 6-kW thermally self-sustained two-stage CO_2 methanation reactor: design and experimental evaluation of steady-state performance under full-load conditions. Applied Energy. 2022;325:119773.
[99] Marinič D, Likozar B. Direct air capture multiscale modelling: From capture material optimization to process simulations. Journal of Cleaner Production. 2023;408:137185.
[100] Surkatti R, Abdullatif YM, Muhammad R, Sodiq A, Mroue K, Al-Ansari T, et al. Comparative analysis of amine-functionalized silica for direct air capture (DAC): Material characterization, performance, and thermodynamic efficiency. Separation and Purification Technology. 2025;354:128641.
[101] She X, Wang X, Han P, Li Y, Wang C. Enhancement of efficiencies of cryogenic energy storage packed bed using a novel Referred-Standard-Volume optimization method. Int J Heat Mass Tran. 2024;224:125367.
[102] Wu W, Benner J, Luo Z. Developing analytical model for nighttime cooling of internal thermal mass. Appl Therm Eng. 2023;220:119798.
[103] Hefti M, Joss L, Bjelobrk Z, Mazzotti M. On the potential of phase-change adsorbents for CO_2 capture by temperature swing adsorption. Faraday Discuss. 2016;192:153-79.
[104] Darunte LA, Sen T, Bhawanani C, Walton KS, Sholl DS, Realff MJ, et al. Moving beyond adsorption capacity in design of adsorbents for CO_2 capture from ultradilute feeds: Kinetics of CO_2 adsorption in materials with stepped isotherms. Industrial & Engineering Chemistry Research. 2018;58:366-77.
[105] Pai KN, Baboolal JD, Sharp DA, Rajendran A. Evaluation of diamine-appended metal-organic frameworks for post-combustion CO_2 capture by vacuum swing adsorption. Separation and Purification Technology. 2019;211:540-50.
[106] Ozkan M, Akhavi A-A, Coley WC, Shang R, Ma Y. Progress in carbon dioxide capture materials for deep decarbonization. Chem. 2022;8:141-73.
[107] Zhang Z, Ding Q, Cui J, Cui X, Xing H. High and selective capture of low-concentration CO_2 with an anion-functionalized ultramicroporous metal-organic framework. Science China Materials. 2020;64:691-7.
[108] Shi WK, Zhang XJ, Liu X, Wei S, Shi X, Wu C, et al. Temperature-vacuum swing adsorption for direct air capture by using low-grade heat. Journal of Cleaner Production. 2023;414:137731.
[109] Stoots CM, O'Brien JE, Herring JS, Hartvigsen JJ. Syngas production via high-temperature coelectrolysis of

steam and carbon dioxide. Journal of Fuel Cell Science and Technology. 2009;6.
[110] Menon V, Fu Q, Janardhanan VM, Deutschmann O. A model-based understanding of solid-oxide electrolysis cells (SOECs) for syngas production by H_2O/CO_2 co-electrolysis. Journal of Power Sources. 2015;274:768-81.
[111] Menon V, Janardhanan VM, Deutschmann O. Modeling of solid-oxide electrolyser cells: From H_2, CO electrolysis to co-electrolysis. ECS Transactions. 2013;57:3207-16.
[112] Petipas F, Brisse A, Bouallou C. Model-based behaviour of a high temperature electrolyser system operated at various loads. Journal of Power Sources. 2013;239:584-95.
[113] Henke M, Willich C, Kallo J, Friedrich KA. Theoretical study on pressurized operation of solid oxide electrolysis cells. International Journal of Hydrogen Energy. 2014;39:12434-9.
[114] Kotas TJ. Basic exergy concepts. In: Kotas TJ, editor. The exergy method of thermal plant analysis: Butterworth-Heinemann; 1985. p. 29-56.
[115] Esmaeilion F, Soltani M, Nathwani J, Al-Haq A, Dusseault MB, Rosen MA. Exergoeconomic assessment of a high-efficiency compressed air energy storage system. Renewable and Sustainable Energy Reviews. 2024;191:114143.
[116] Liu Z, Liu Z, Yang X, Zhai H, Yang X. Advanced exergy and exergoeconomic analysis of a novel liquid carbon dioxide energy storage system. Energ Convers Manage. 2020;205:112391.
[117] Kianfard H, Khalilarya S, Jafarmadar S. Exergy and exergoeconomic evaluation of hydrogen and distilled water production via combination of PEM electrolyzer, RO desalination unit and geothermal driven dual fluid ORC. Energ Convers Manage. 2018;177:339-49.
[118] Akrami E, Chitsaz A, Nami H, Mahmoudi SMS. Energetic and exergoeconomic assessment of a multi-generation energy system based on indirect use of geothermal energy. Energy. 2017;124:625-39.
[119] Bashiri Mousavi S, Ahmadi P, Hanafizadeh P, Khanmohammadi S. Dynamic simulation and techno-economic analysis of liquid air energy storage with cascade phase change materials as a cold storage system. J Energy Storage. 2022;50:104179.
[120] Habibollahzade A, Gholamian E, Behzadi A. Multi-objective optimization and comparative performance analysis of hybrid biomass-based solid oxide fuel cell/solid oxide electrolyzer cell/gas turbine using different gasification agents. Applied Energy. 2019;233-234:985-1002.
[121] Couper JR, Penney WR, Fair JR. Chemical process equipment: Selection and design. 2nd ed. Massachusetts: Elsevier; 2012.
[122] Gorre J, Ruoss F, Karjunen H, Schaffert J, Tynjälä T. Cost benefits of optimizing hydrogen storage and methanation capacities for Power-to-Gas plants in dynamic operation. Applied Energy. 2020;257:113967.
[123] Razmi AR, Janbaz M. Exergoeconomic assessment with reliability consideration of a green cogeneration system based on compressed air energy storage (CAES). Energ Convers Manage. 2020;204:112320.
[124] Kurşun B. Comparison with Carnot battery of an alternate thermal electricity storage charged by concentrated photovoltaic thermal system and resistance heater. Appl Therm Eng. 2025;258:124587.
[125] Li Y, Alsenani TR, Asiri M, Ayadi M, Ooi JB, Chammam W. Thermodynamic and economic assessments of an innovative methane liquefaction and multigeneration process relying on coke oven gas flow and micro gas turbine cycle. International Journal of Hydrogen Energy. 2025;138:1017-33.
[126] Jannelli E, Minutillo M, Cozzolino R, Falcucci G. Thermodynamic performance assessment of a small size CCHP (combined cooling heating and power) system with numerical models. Energy. 2014;65:240-9.
[127] Gruber M, Weinbrecht P, Biffar L, Harth S, Trimis D, Brabandt J, et al. Power-to-Gas through thermal integration of high-temperature steam electrolysis and carbon dioxide methanation - Experimental results. Fuel Processing Technology. 2018;181:61-74.